ALMA MATER STUDIORUM · UNIVERSITÀ DI BOLOGNA

Scuola di Scienze
Corso di Laurea Magistrale in Fisica

SURFACE PREPARATION AND CHARACTERIZATION OF SEMIPOLAR (20-21) INGAN LAYERS

Relatore:
Prof.ssa Daniela Cavalcoli

Presentata da:
Julian Plaickner

Correlatore:
Prof. Patrick Vogt

Sessione III
Anno Accademico 2012/2013

Index

Abstract iii

Introduction 1

Chapter 1 – Overview on nitride semiconductors

1.1 Crystal structure . . . 3
1.2 Polarity . . . 4
1.3 Polarization fields . . . 6
1.4 Energy gap . . . 8
1.5 Surface electron accumulation . . . 9
1.6 Heteroepitaxial growth . . . 11

Chapter 2 – The semipolar (20-21) surface

2.1 Surface reconstructions . . . 15
2.2 Morphology of (20-21)-GaN samples . . . 17
2.3 Semipolar GaN substrates . . . 19
2.4 Indium incorporation and critical thickness . . . 21
2.5 Semipolar InGaN LEDs . . . 23

Chapter 3 – Surface-analytic experimental techniques

3.1 Surface physics . . . 27
3.1.1 General considerations . . . 28
3.1.2 Ultra high vacuum (UHV) . . . 28
3.1.3 Surface preparation . . . 30
3.2 Electron spectroscopy . . . 30
3.2.1 X-ray Photoelectron Spectroscopy (XPS) . . . 31
3.2.2 Interpretation of XPS spectra . . . 33
3.2.3 Auger Electron Spectroscopy (AES) . . . 35
3.3 Scanning probe microscopy (SPM) . . . 37
3.3.1 Working principle of SPM . . . 37
3.3.2 Atomic force microscopy (AFM) . . . 38
3.3.3 Scanning tunneling microscopy (STM) . . . 40
3.4 Surface Photovoltage Spectroscopy (SPS) . . . 42
3.5 Low energy electron diffraction (LEED) . . . 45

Chapter 4 – Surface preparation and structural properties

4.1 Properties of studied InGaN samples 47
4.2 Morphology of oxidized surface 48
4.3 Thermal annealing 50
4.4 Stoichiometry 52
4.5 Polarity determination by XPS 53
4.6 Surface reconstructions by LEED. 55

Chapter 5 – Electronic and optical properties

5.1 Calibration of STM on HOPG films 57
5.2 STM images of the InGaN samples. 59
5.3 Band bending 61
5.4 SPS measurements. 64
5.5 STS measurements. 70
5.6 Optical transmission studies 72

Summary and conclusions **75**

References **77**

Acknowledgment **81**

Abstract

In questa tesi vengono studiate le proprietà fisiche della superficie di eterostrutture InGaN/GaN cresciute con orientazione semipolare (20-21). Questi materiali fornirebbero una valida alternativa alle eterostrutture cresciute secondo la tradizionale direzione di crescita polare (0001) per la realizzazione di LED e diodi laser. I dispositivi cresciuti con orientazione semipolare (20-21) sono studiati soltanto da pochi anni e hanno già fornito dei risultati che incitano significativamente il proseguimento della ricerca in questo campo. Oltre all'ottimizzazione dell'efficienza di questi dispositivi, sono richieste ulteriori ricerche al fine di raccogliere delle informazioni mancanti come un chiaro modello strutturale della superficie (20-21).
I capitoli 1 e 2 forniscono un quadro generale sul vasto campo dei semiconduttori basati sui nitruri del terzo gruppo. Il capitolo 1 tratta le proprietà generali, come le caratteristiche della struttura cristallina della wurtzite, l'energy gap e il più comune metodo di crescita epitassiale. Il capitolo 2 tratta le proprietà specifiche della superficie (20-21) come struttura, morfologia e proprietà legate all'eterostruttura InGaN/GaN (incorporazione di indio, strain e spessore critico).
Nel capitolo 3 vengono descritte sinteticamente le tecniche sperimentali utilizzate per studiare i campioni di InGaN. Molte di queste tecniche richiedono condizioni operative di alto vuoto e appositi metodi di preparazione superficiale.
Nel capitolo 4 vengono discussi i risultati sperimentali riguardanti la preparazione superficiale e le proprietà strutturali dei campioni. Il trattamento termico in ambiente ricco di azoto si rivela essere un metodo molto efficiente per ottenere superfici pulite. La superficie dei campioni presenta una morfologia ondulatoria e una cella unitaria superficiale di forma rettangolare.
Nel capitolo 4 vengono discussi i risultati sperimentali relativi alle proprietà elettroniche e ottiche dei campioni. Immagini alla risoluzione atomica rivelano la presenza di ondulazioni alla scala dei nanometri. Vengono misurati l'energy gap e l'incurvamento superficiale della bande. Inoltre vengono identificate una serie di transizioni interbanda dovute all'interfaccia InGaN/GaN.

In this thesis, the physical properties of the surface of semipolar (20-21) InGaN/GaN heterostructures are investigated. These materials should provide an adequate alternative to (0001)-oriented heterostructures for the realization of high efficiency light emitting diodes (LEDs) and laser diodes (LDs). Semipolar (20-21)-oriented devices are studied only by a few years and have already showed good results, providing an incentive to continue the research in this field. In addition to the optimization of the efficiency of the devices, further investigations are required in order to understand remaining issues such as the development of a structural model of the (20-21) surface.

Chapters 1 and 2 give an overview on the extensive field of the III-nitride semiconductors. Chapter 1 deals with the general properties, i.e. structural properties related to the wurtzite crystal structure, the energy gap and the most common heteroepitaxial growth method. Chapter 2 deals with specific properties of the semipolar (20-21) surface (structure and morphology) and of the InGaN/GaN heterostructures (indium incorporation, stress relaxation and critical thickness).

Chapter 3 gives an overview on the experimental surface-analytic techniques used to investigate the InGaN samples. Most of these techniques require ultra-high vacuum conditions and appropriate surface preparation methods.

In chapter 4, we present the experimental results concerning the surface preparation and structural properties of the studied samples. Thermal annealing in nitrogen ambient is found to be a very efficient method to obtain clean InGaN surfaces. The surface of the samples exhibit a undulated morphology and a cubic-like surface unit cell.

In chapter 5 we consider the results concerning the electronic and optical properties. Atomic-resolved images of the surface reveal the presence of undulations at the nanoscale. The energy gap and the surface band bending are measured. Further, a set of interband transitions related to the InGaN/GaN interface are identified.

Introduction

The III-V semiconductors (like AsGa, InP) were systematically investigated since the 1950s: they are also called classical semiconductors. In contrast, the research on III-nitride semiconductors (like GaN, InN) started many years later. This is also due to the fact that growth and physical properties of these materials present many challenges. On the other hand, the so-called III-nitrides in the form of ternary compounds (AlGaN, InGaN, AlInN) offer the opportunity to tune the band gap and hence the emission wavelength of opto-electronic devices such as light emitting diodes (LEDs), laser diodes and photo-detectors over a wide spectral range from the ultra violet over the whole visible region.

Since the demonstration of the first III-nitride light-emitting devices (LEDs) and laser diodes (LDs) in the early 1990s, significant advances has been realized towards increasing device efficiency, improving device reliability and developing advanced device designs for high-power applications [1]. Although progress has been considerable, current commercially available III-nitride LEDs and LDs are still grown on the (0001) c-plane of the wurtzite crystal structure and their performance is nonetheless affected by the presence of polarization-related electric fields. When III-nitride heterostructures are grown along the c-axis, fixed polarization-related sheet charges at interfaces can result in large internal electric fields. These fields can create several issues for III-nitride LEDs and LDs, including reductions in the radiative combination rate due to spatial separation of the electron and hole wavefunctions, i.e. phenomenon referred to as Quantum Confined Stark Effect (QCSE), and blueshifts in the peak emission wavelength with increasing carrier density.

In 2000, Waltereit et al clearly demonstrated the absence of internal electric fields in m-plane GaN quantum wells, triggering a worldwide research effort in nonpolar and semipolar III-nitride semiconductors [1]. In addition to the significant reduction of the polarization fields, the growth of nitride heterostructures along non- and semipolar orientations yields a number of new design options to control the optoelectronic properties of the light emitters. Today, the understanding of polar, semipolar and nonpolar nitrides has made leaps forward. However, there is a wide range of topics related to the III-nitrides like growth and heteroepitaxy, theory and modeling, optical and electronic properties, and there remains still challenges and open issues [2].

These studies are of major importance for the role played by InGaN in many optoelectronic applications. Group-III nitride based laser diodes

and light emitting devices in the visible spectrum employ InGaN quantum wells as active regions. Several crystal orientations for the growth of InGaN quantum wells are of interest for such devices. The technological setup for the realization of InGaN based heterostructures and devices has been developed only recently and the efficiency of these devices depends on several factors like growth quality, crystal orientation and surface preparation. Therefore, there still remain a variety of experimental investigations to perform in order to obtain an adequate overview on efficiency and properties of such devices.

Chapter 1
Overview on nitride semiconductors

In this chapter, a brief overview on III-nitride semiconductors is given. Beside of structure-dependent properties related to the wurtzite crystal structure such as polarity and polarization fields, widely treated in literature, also the recently studied phenomenon of surface electron accumulation is considered. The most common heteroepitaxial growth method of III-nitrides is described. The properties of III-nitrides which are related in a specific way to the semipolar (20-21) crystal orientation are reported in chapter 2.

1.1 Crystal structure

III-nitride semiconductor compounds crystallize in either the hexagonal wurtzite structure or in the cubic zincblende structure (figure 1.1), which are closely related to each other. In both cases, each group-III atom is tetrahedrally coordinated by four nitrogen atoms. The main difference between the two crystal structures is the stacking sequence of the close packed diatomic planes. The stacking sequences are ABABAB along the wurtzite [0001] directions and ACBACB along the zincblende [111] directions. This difference results in distinct space group symmetries,

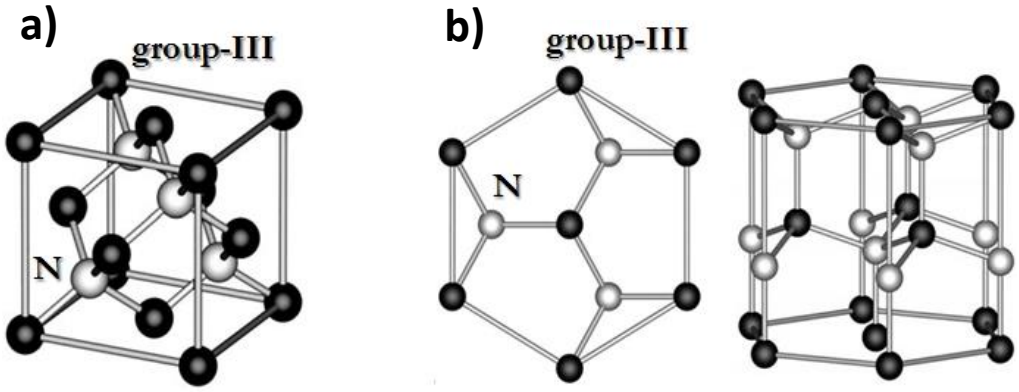

FIG. 1.1. Unit cell of III-nitrides with a) zincblende and b) wurtzite crystal structure (top view and side view) [3].

$P6_3mc$ for wurtzite and F43m for zincblende [4]. Wurtzite structure consists of two embedded hexagonal atom stacks along the [0001]-

direction and is also called hexagonal closest packings (hcp). To indicate direction, axis and planes of the wurtzite crystal structure, a modified Miller-Bravais notation {hkil} is employed, where i = -(h+k). When h = k = i = 0 and l = 1, then this (0001) plane is called c-plane and the perpendicular direction to this plane is called c-direction or [0001] [5].

The c-plane of wurtzite III-nitrides is also called polar plane, whereas the other crystal planes are called semi-polar or non-polar planes (figure 1.2). In contrast to the polar structure of III-nitrides, the semi-polar

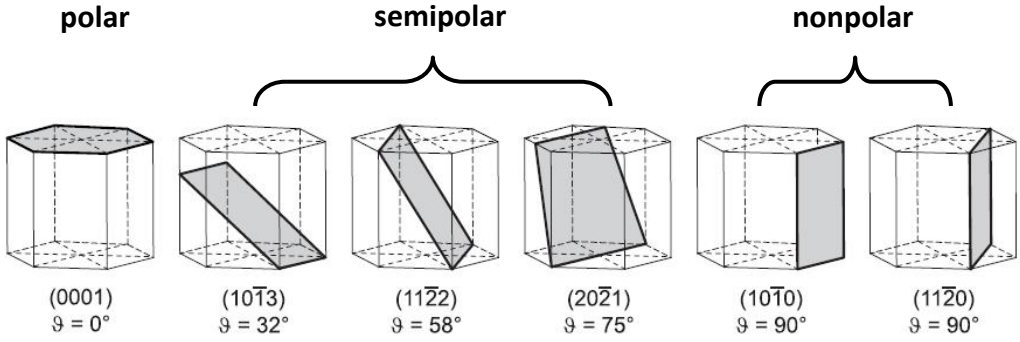

FIG. 1.2. Different crystallographic orientations in the wurtzite unit cell [6].

and non-polar structures exhibit two-fold surface symmetry instead of the six-fold symmetry: this has an impact on many physical properties of the material. For example, the microstructure of nonpolar and semipolar heteroepitaxial films is drastically different from that of films deposited along the polar direction. A different microstructure gives rise to different type of defects from which electrical and optical properties depend.

1.2 Polarity

An important structural property is the polarity, a term that refers to the atoms lying at the topmost of the bare layer surface, i.e. the surface with the least number of broken bonds. For III-nitrides the surface can be N-polar or group-III-polar. It's important to distinguish between polarity and surface termination. As clarified by the example showed in figure 1.3, the same atom can lie at the topmost of the surface for two different polarities. The polarity of III-nitrides depends on the growth conditions. Polarity control of III-nitrides is an important issue, on which thermal and optical properties, as well as chemical and internal stability strongly depend.

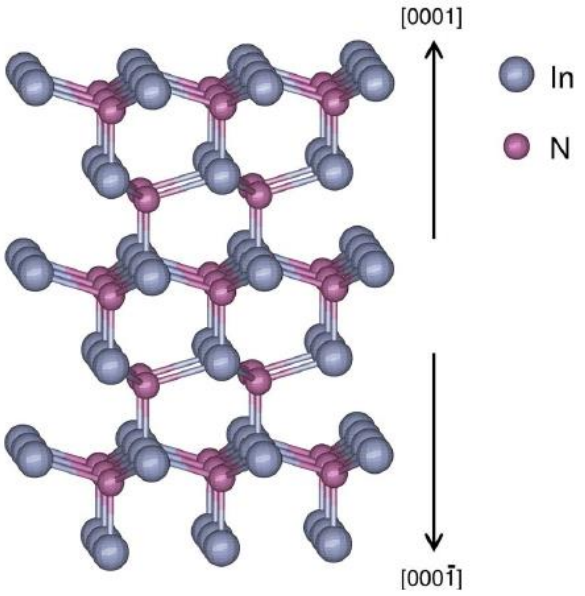

FIG. 1.3. Ball and stick model illustrating the In-polarity [0001] and the N-polarity [000-1] directions of the wurtziteInN. The surfaces are both shown with In termination [7].

The commonly used methods for InN and GaN polarity determination are convergent beam electron diffraction (CBED) [8] and wet etching [9]. Nevertheless, these methods have some limitations. The thickness and crystal quality of the investigated layers must be sufficiently high to achieve clear diffraction spots, required for polarity determination by CBED. In the case of wet etching, different crystal facets may etch slower or faster leading to difficulties in polarity determination. As reported recently by D. Skuridina et al. [10], X-ray Electron Spectroscopy (XPS) is a suitable technique for polarity determination of InN and GaN layers with different surface orientations (0001), (000-1) and (11-22). The method is based on the observation of a peak preference in the valence band (VB) spectrum:

- The peak at lower binding energy is mainly associated with p-like orbital states and dominates for group-III polar samples.
- The peak at higher binding energy has a partial contribution of s-like states and dominates for N-polar samples.

In comparison to other polarity determination methods, Polarity determination by XPS is non-destructive and also suitable for oxidized layers with rough surface.
The fact that photoelectrons emitted from the surface are affected by the polarization field in the crystal might explain the origin of the differences in VB states at low and high binding energies. The presence of a

polarization field is related to the wurtzite crystal symmetry (as explained in section 1.3) and also to the large electronegativity difference between nitrogen and group-III atoms. However, similar peak dependences of the VB states with respect to the crystal polarity were observed also for wurtzite II-VI semiconductors, such as ZnO and CdS [11]. The origin of the correlation between VB peak and crystal polarity is not yet fully understood.

1.3 Polarization fields

The presence of polarization is strongly connected to the unit cell symmetry of the crystal. In the absence of external electric fields, the total macroscopic polarization of a solid is the sum of the spontaneous polarization of the equilibrium structure and of the strain-induced piezoelectric polarization.

The zincblende compound semiconductors have four symmetry equivalent polar axes whose contributions cancel each other in equilibrium. Hence, these materials don't exhibit a spontaneous polarization. In contrast, the wurtzite structure has a singular polar axis, the c-axis, along which the structure exhibit a spontaneous polarization. Semiconductor layers are often grown under strain due to the lattice mismatch to the underlying layer. The strain produces a deformation of the unit cell which can lead to an additional polarization. In the case of the zincblende, the growth along one of the polar axes lift the symmetry and the crystal exhibit therefore a piezoelectric polarization. The wurtzite structure with its unique polar axis always carries piezoelectric polarization for any growth direction [4].

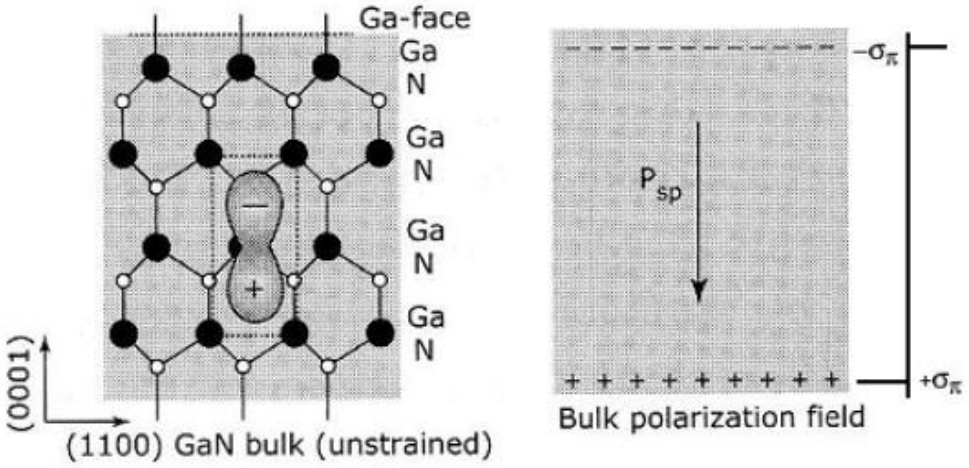

FIG. 1.4. Microscopic picture of spontaneous polarization in a free-standing GaN slab [4].

A way to illustrate the spontaneous polarization is showed in figure 1.4. Each unit cell can be thought to contain a charge dipole that is formed due to the spatial separation of the barycenter of the negative charges (electron clouds) and the positive charges (atomic nuclei). The dipoles in every layer of unit cells neutralize each other in the bulk of the semiconductor, but form sheet charges on the surfaces. A free Ga-face surface develops a negative sheet charge and a positive sheet charge forms on the N-face. The surface polarization charge density for GaN is of the order of 10^{13} cm^{-2}. These charges are large enough to affect the electrical properties of a material drastically at surfaces and interfaces. Since the atomic sheet density in nitride semiconductors is 10^{15} cm^{-2}, roughly 1% of the atoms contribute to the polarization charge.

The phenomenon of polarization is important for applications in microelectronics. For example, the spontaneous polarization generate a two-dimensional electron gas (2DEG) in a AlInN/GaN heterostructure sand this gives rise to high performance high electron mobility transistors (HEMTs) [12]. The knowledge of the polarization component ΔP_z along the growth direction is also important for the understanding of the behavior of optoelectronic devices. This component was calculated under the assumption of full strained epitaxial layers by Romanov et al. [13].

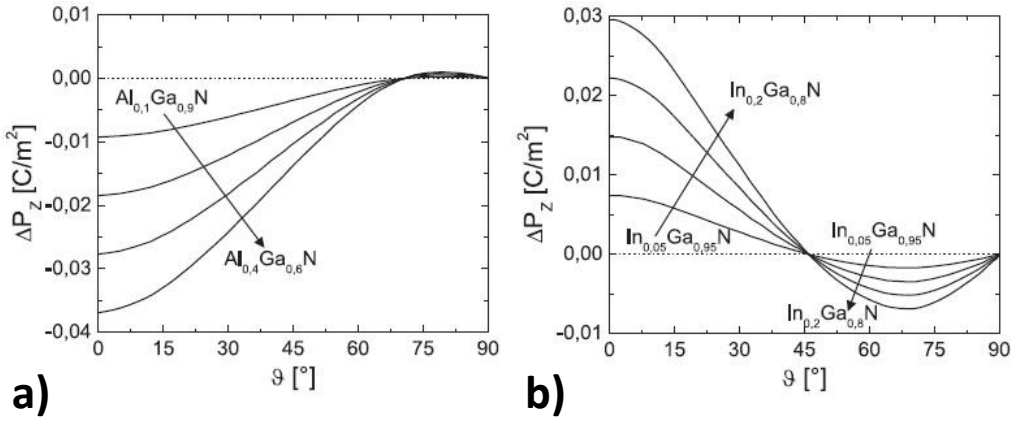

FIG. 1.5. Polarization component along growth direction as function of the angle between growth direction and c-direction for a) AlGaN and b) InGaN on a GaN substrate [6].

ΔP_z is shown as function of the angle between growth direction and c-direction in figure 1.5. ΔP_z is maximal for growth along the c-direction and is reduced for every different growth orientation. It vanishes at two different angles, which are influenced in a very small extent by the alloy composition.

1.5 Energy gap

Early optical absorption studies on sputtered InN films suggested a fundamental gap of 1.9 eV. However, further measurements on InN films grown by Molecular Beam Epitaxy (MBE) indicated a fundamental gap of 0.7 eV. Therefore, it has become necessary to reevaluate many of the material parameters of InN and the composition dependence of the bandgap of all group-III nitride alloys. In fact, the discovery of the narrow bandgap of InN has extended the spectral range of the group III-nitride ternary alloy system, which can now be tuned from the near infrared at 0.7 eV to the deep ultra-violet at 6.2 eV. This wide spectral range offers novel possibilities for the use of group-III nitrides in a variety of device applications. For instance, the energy gaps available in the InGaN alloy system provide an almost perfect match with the full solar spectrum, which makes InGaN a potential material for high efficiency multi-junction solar cells [14].

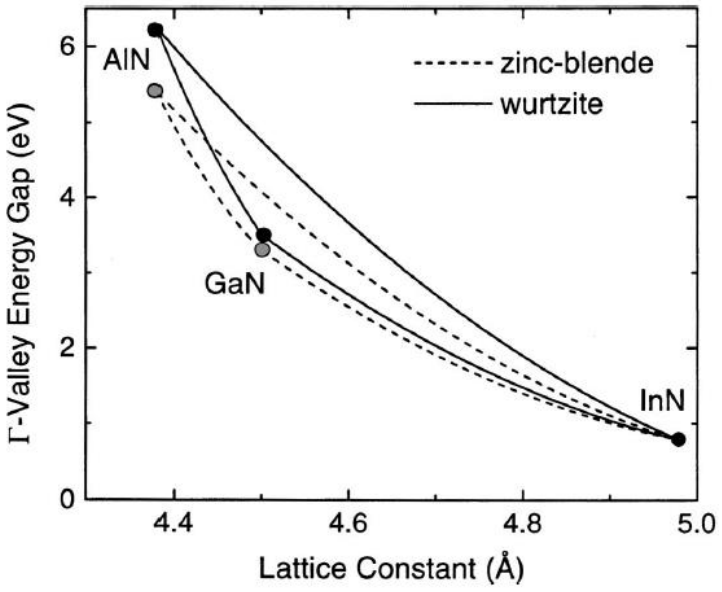

FIG. 1.7. Energy gap of wurtzite (solid curves) and zincblende (dashed curves) nitride semiconductor alloys and binaries (points) [15].

The energy gaps of wurtzite and zincblende nitride semiconductor alloys are plotted in figure 1.7 as function of lattice constant. A more detailed study of the bandgap is reported in more recent works [16]. The

composition dependences of the energy gaps for the ternary alloys AlGaN, InGaN, AlInN satisfy the quadratic form

$$E_g(A_{1-x}B_x) = (1-x)E_g(A) + xE_g(B) - bx(1-x)$$

where the so-called bowing parameter b accounts for the deviation from a linear interpolation between the two binaries A and B. The bowing parameter is always positive for these materials, which reflects a reduction of the alloy energy gaps. Up to now, no agreement has been reached on the bowing parameter value and even on the issue if a single bowing parameter can describe the gaps over its entire composition range [17].
The temperature dependence of the energy gap is usually parameterized using the semi-empirical Varshni formula

$$E_g(T) = E_g(T=0) - \frac{\alpha T^2}{T+\beta}$$

where α and β are independent parameters that are specific to each system. These parameters are generally sufficient to describe the conduction and valence band structures of bulk nitride materials [15]. However, as the growth conditions and sample structure vary from one sample to another, the reported values for α and β in literature cannot be generalized to characterize a given semiconductor compound. Here one of the major problems arises from the heteroepitaxial relationship between substrate and nitride layers. Since epitaxially grown heterostructures routinely combine layers of lattice-mismatched constituents, the material properties under strain must also be specified. This is conventionally done within the deformation potential theory.

1.6 Surface electron accumulation

In a compound semiconductor, at a certain energy, called the branch-point energy, the valence band (VB) and the conduction band (CB) states change their character from donor-like to acceptor-like. If we have a low Γ-point conduction band minimum (CBM) with respect to the branch-point energy we speak about surface electron accumulation [5]. This phenomenon has attracted much attention since a high surface electron density implies a great technological importance. Surface electron accumulation was observed to be an intrinsic property of InN with different surface orientations [18], [19]. For InGaN and AlInN alloys, a transition from

electron accumulation to electron depletion was observed. The mean reason of the appearance of electron accumulation on the surface of InN and related alloys was attributed to In-In metallic bonds, leading to occupied surface states above the CBM.

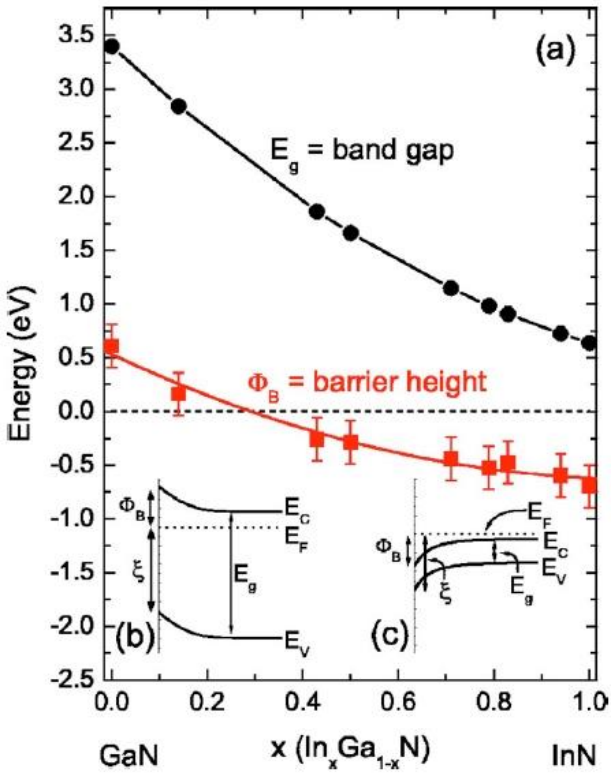

FIG.1.8. Variation of bandgap and barrier height at (0001)-InGaN surfaces with different indium concentrations in presence of a native oxide. Insets (b) and (c) depict the upward band bending in a depletion layer at a GaN surface and the downward band bending in an accumulation layer at an InN surface, respectively [20].

The composition dependence of the Fermi-level position with respect to the band edges for oxidized (0001) surfaces of n-type InGaN films was investigated using x-ray photoemission spectroscopy (XPS) by Veal et al [20]. The surface Fermi-level position varies from high above the CBM at InN surfaces to significantly below the CBM at GaN surfaces. The surface preparation would require a different method to be optimized for each InGaN composition, consequently, the composition dependence of the Fermi-level pinning has been studied in the presence of the native oxide on the surfaces. The separation between CBM and surface Fermi level, called barrier height Φ_B, has been determined from the photoemission data (shown in figure 1.8).

Two possible situations occur:

- $\Phi_B > 0$: Fermi level pinning in the band gap
- $\Phi_B < 0$: Fermi level pinning within the conduction band

The composition dependence of the barrier height is estimated by the least squares method to be

$$\Phi_B = 0.95x^2 - 2.1x + 0.53$$

From this equation it can be found that the barrier height is zero, i.e. the surface Fermi level coincides with the CBM, at x = 0.29. This composition does not necessarily coincide with the transition from surface electron depletion to accumulation as the nature of the space charge region is determined in a particular sample by whether the bulk Fermi level is above or below the surface Fermi level. However, it is expected that the transition occurs at a value quite close to the zero of the barrier height.

The knowledge of the surface Fermi level is important for surface sensitive devices, such as chemical and biological sensors, where an InGaN active layer is exposed to the environment.

1.7 Heteroepitaxial growth

The growth of high quality epitaxial layers, i.e. layers with a smooth morphology and a low defect density, is the basis for fundamental study and device fabrication. In recent years, the most suitable growth technique for III-nitrides has been found to be Metal Organic Vapor Phase Epitaxy (MOVPE). MOVPE growth is conducted under near thermodynamic equilibrium conditions which rely on vapor transport of precursors in a heated zone. In order to create there near equilibrium conditions, a substrate is typically located on a heated susceptor in the heated zone. The growth occurs via the decomposition of the precursors over the heated substrates. During growth, several processes like adsorption, surface migration and chemical reactions occur. A picture of the processes involved during MOVPE growth is illustrated in figure 1.9.

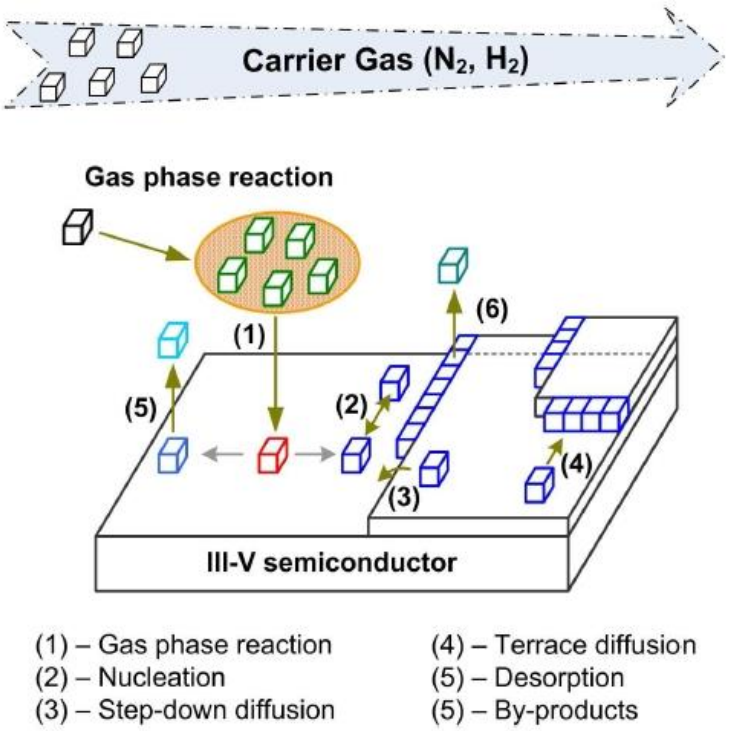

FIG. 1.9. Scheme of the surface processes involved during the MOVPE growth [5].

Basically, there are six reaction steps during the MOVPE growth, which occur simultaneously:

1. Transport of the precursor molecules from the sources to the heated zone.
2. The species resulting from the gas phase decomposition can diffuse on the surface and incorporate into the layer.
3. Terrace diffusion
4. Step-down diffusion (significant only a high temperature)
5. Desorption
6. By-products processes

For the complex MOVPE system the overall reaction rate in the reactor is controlled by:

- **Thermodynamics:** determines the driving force and the direction of the reaction
- **Kinetics:** determines the rates of change in the concentration of reactants in the chemical reaction

- **Hydrodynamics:** determines fluid flow, heat transfer and chemical transport of species

Because of the dependence on the thermal decomposition of the precursors, the MOVPE growth process strongly depends on growth temperature and on the amount of the precursors. A qualitative picture of the effect of substrate temperature and reactor pressure on growth rate of the layer is shown in figure 1.10. At very high growth temperature, desorption is dominating.

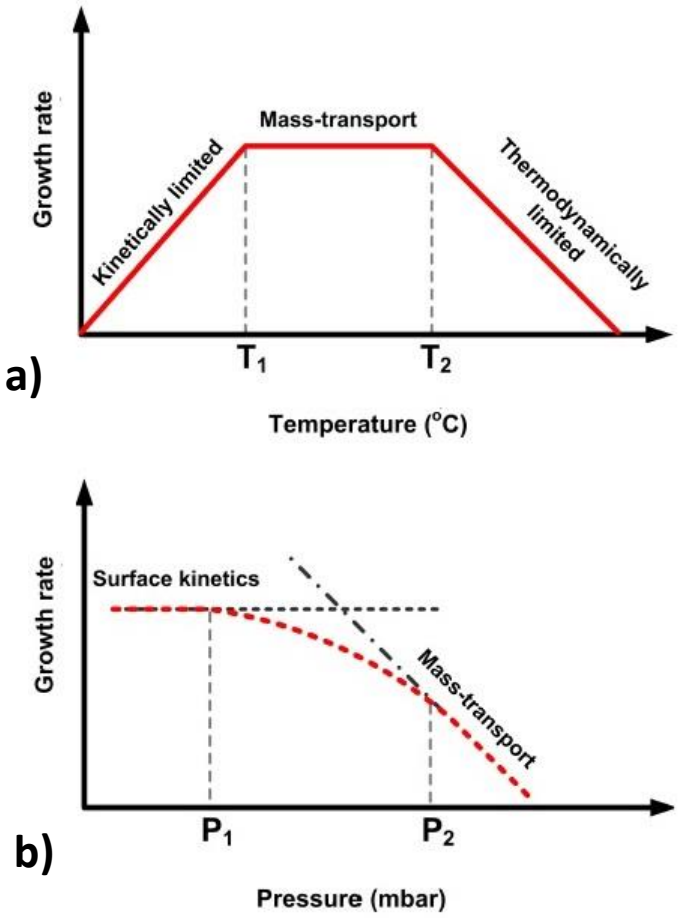

FIG. 1.10. Qualitative picture of the effect of a) substrate temperature and b) reactor pressure on growth rate of the layer [5].

If the growth temperature is very low, the decomposition of precursors is less and hence the growth rate decreases. The stability of the group-III precursors is very important since it decides which growth temperature is necessary for epitaxy. Morphology and structure of the epitaxial layer depend strongly on the growth conditions, i.e. temperature, precursor and substrate. All of them contribute to different morphologies and structures

of the grown layers. The growth process of the layer might be followed different growth modes. The growth of epitaxial layers on a single crystal surface depends significantly on the interaction strength between atoms and the surface.
In the choice of the substrate for the growth of III-nitrides, different aspects should be taken into account:

- **Thermal expansion and lattice mismatches:** they strongly affect growth process and quality of epitaxial layers,
- **Thermal stability:** an easily decomposed substrate at high temperature might be a source for unintentionally contaminations in epitaxial layers
- **Polarity:** the polarity of the substrate leads to growth of different polarity of epitaxial layer.

The control of growth orientation is very important since on which structure, morphology, electrical and optical properties strongly depend. III-nitrides having different polarities shows different thermal stability and different amount of contaminations. Despite the high lattice mismatch respect to III-nitrides, sapphire is still most a widely used substrate due to a low-cost production, thermal stability and easy handling. Generally, III-nitride layers grown on c-plane sapphire will have the c-growth-direction. However, due to different crystal structures between III-nitrides and other planes of sapphire, it is very difficult do control semi- and non-polar growth orientations of III-nitrides on sapphire.
In contrast to sapphire substrate, the other group III-nitrides are good candidates for substrate selections since they have the same crystal structure and much smaller lattice and thermal mismatches compared to sapphire. Generally, the overgrown layer on the other III-nitride substrates reproduces the crystal orientation and the polarity of the substrates. However, production and preparation of free-standing III-nitride substrates is difficult due to the cost [5].

Chapter 2
The semipolar (20-21) surface

In this chapter we will consider specific properties of the semipolar (20-21) surface, focusing on structural and morphological properties of (20-21)-GaN. After this, the properties of InGaN/GaN heterostructures such as indium incorporation and critical thickness are reported, with a final impression on a typical application, i.e. a semipolar InGaN LED.
It is reasonable to expect that the main surface properties of the semipolar (20-21)-InGaN samples investigated in this thesis are similar to those of GaN samples with the same orientation. First, the InGaN samples exhibit a low indium content, thus representing, roughly speaking, a kind of perturbation of a GaN sample. Second, the InGaN layers are very thin and are grown on a semipolar (20-21)-GaN substrate, so that we expect that structural properties of the substrate are transferred to the top layer.

2.1 Surface reconstructions

Conceptually, a surface is obtained by cutting a solid: the separation will coincide with a crystallographic hkl-plane. This operation has two important consequences:

1) The three-dimensional symmetry of the crystal lattice is broken
2) Due to unsatured chemical bonds, the total energy of the hkl-plane associated with the surface is higher than the energy of the same hkl-plane inside the solid.

First, on a surface, due to the absence of neighboring atoms on one side, there are different interatomic forces in the uppermost lattice. Therefore, the equilibrium conditions for surface atoms are modified with respect to the bulk; one therefore expects altered atomic positions. Second, as in any physical system occurs, the surface will tend to minimize its energy. This minimization process can be obtained through atomic rearrangements.

There are different types of atomic rearrangements. We consider here just the main two types, which are called relaxation and reconstruction and are schematically illustrated in figure 3.1. In a relaxation, the top few interlayer separations normal to the surface are changed. More dramatic changes are involved in a surface reconstruction, where the lattice

periodicity is altered because the atoms are subjected to shifts parallel to the surface. Semiconductor surfaces with their strongly directional covalent

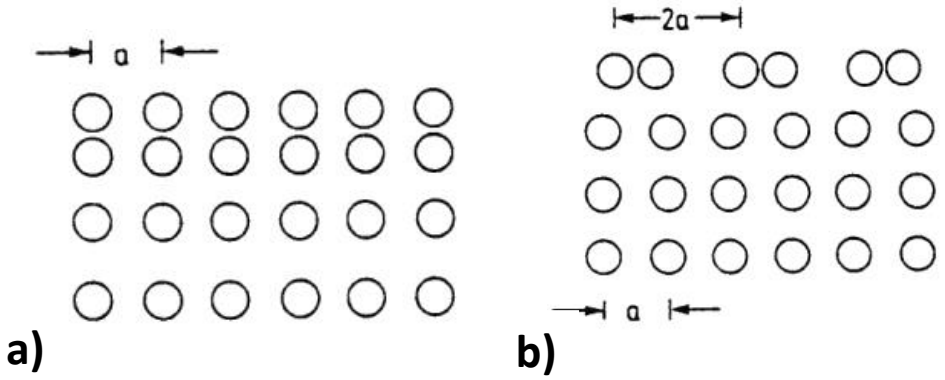

FIG. 2.1. Simple schematic representation of a) relaxation and b) surface reconstruction [21].

bonding character often show quite complex reconstructions. A variety of experimental methods, such as LEED (low energy electron diffraction), ARUPS (angle resolved ultraviolet photoelectron spectroscopy) and RBS (Rutherford back-scattering), are today available to investigate surface reconstructions.

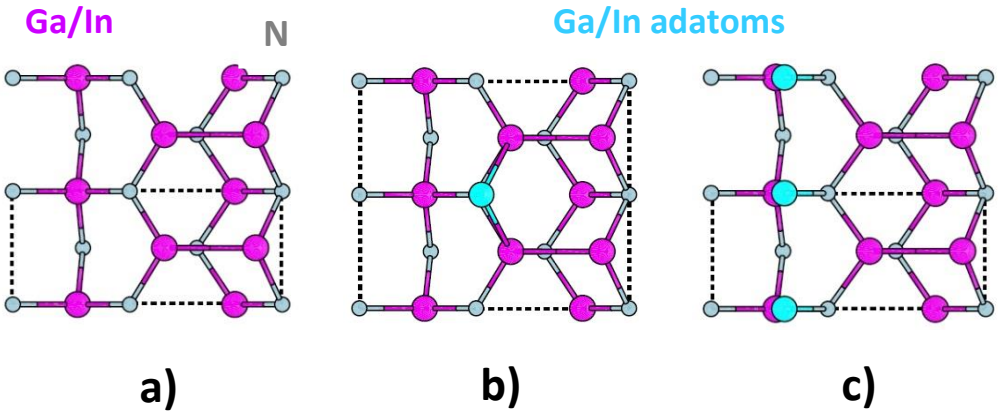

FIG. 2.2. Schematic of top view of a) N-desorbed surface (stable under N-rich conditions), b) 1x2 N-desorbed surface with metallic adatom (stable under moderate Ga-rich conditions), c) metallic adlayer (stable under extreme Ga-rich conditions) [22].

Yamashita et al. [22] investigated the reconstructions on (20-21)-GaN and (20-21)-InN surfaces on the basis for first-principles total energy calculations (pseudopotential approach with generalized gradient approximation). The calculated surface formation energy revealed that the

reconstructions depend on the chemical potential of Ga for the (20-21)-GaN surface, while the surface with an In adlayer is stabilized regardless of the growth conditions for the (20-21)-InN surface. The relative stability among the various reconstructions is discussed in figure 2.2. For GaN, the surface where topmost N atoms are desorbed is stable under N-rich conditions, while a metallic reconstruction is stabilized under Ga-rich conditions.

2.2 Morphology of (20-21)-GaN surfaces

Because of the reduced surface symmetry, semipolar GaN surfaces doesn't exhibit monoatomic steps like in the case of polar (0001)-GaN surfaces. The GaN layers grown on semipolar GaN substrates exhibit a kind of long

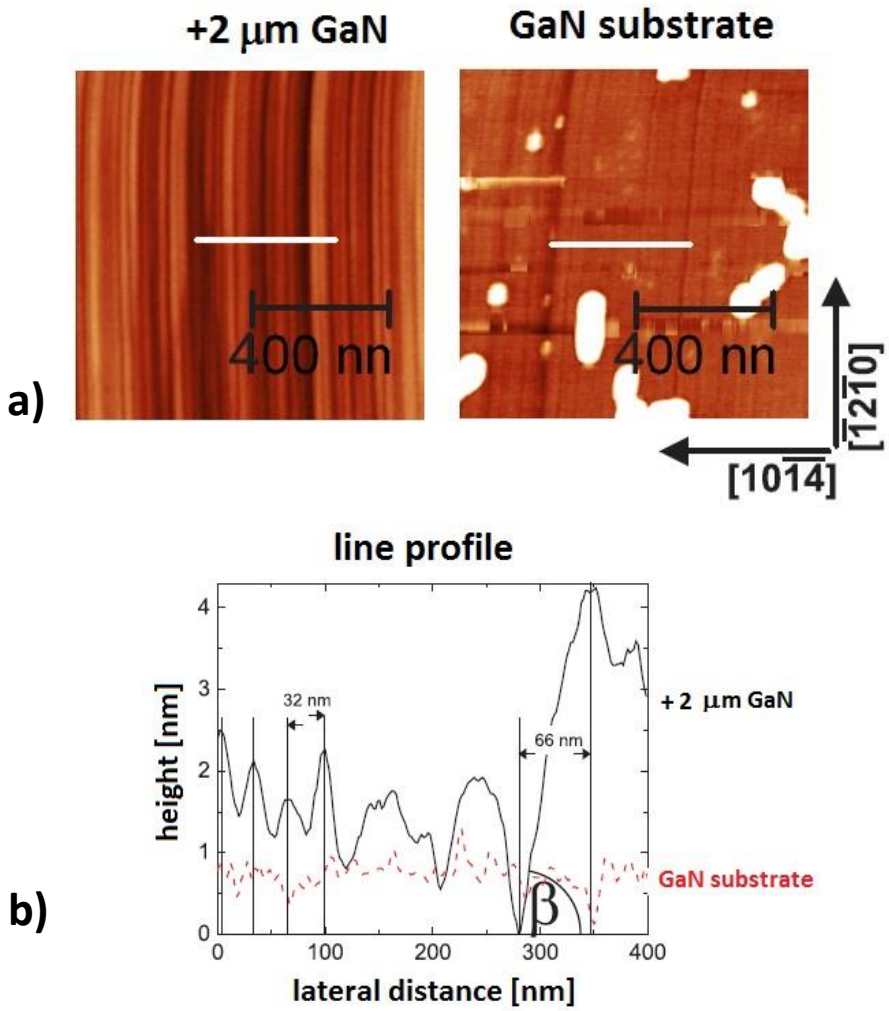

FIG. 2.3. a) Topography of a semipolar (20-21)-GaN layer. The white spots on the surface of the GaN substrate are probably related to impurities in the growth chamber; b) line profiles corresponding to the white lines in a) [6].

structures with arrow-similar extremities. The structures observed on semipolar surfaces can be described in a simple way as undulations [6]. In the case of the (20-21)-GaN surface, undulations along the [10-1-4] direction with period between 20 nm and 40 nm are observed. Evidently, the morphology of the GaN substrate is transferred to the GaN overgrown epitaxial layer. Under certain growth conditions, for example 1015 °C and 150 hPa, one can distinguish a second kind of undulation with greater amplitude, as shown in fig 2.3b. Line profiles show that the cause lies in the random stacking of the undulations. This stacking is referred to as undulation bunching.

A study of the relation between surface morphology and growth parameters (shown in figure 2.4) elucidates that both the undulation bunching and the undulation amplitude increase with temperature and with reactor pressure. This is observed in both type of MOVPE reactors, the horizontal reactor and the vertical reactor (further details about the growth conditions are reported elsewhere [6]). The surfaces with the lowest roughness, i.e. with a roughness around 0.3 nm, were obtained at 950 °C and 50 hPa and with a V/III ratio around 3000. The observed morphology

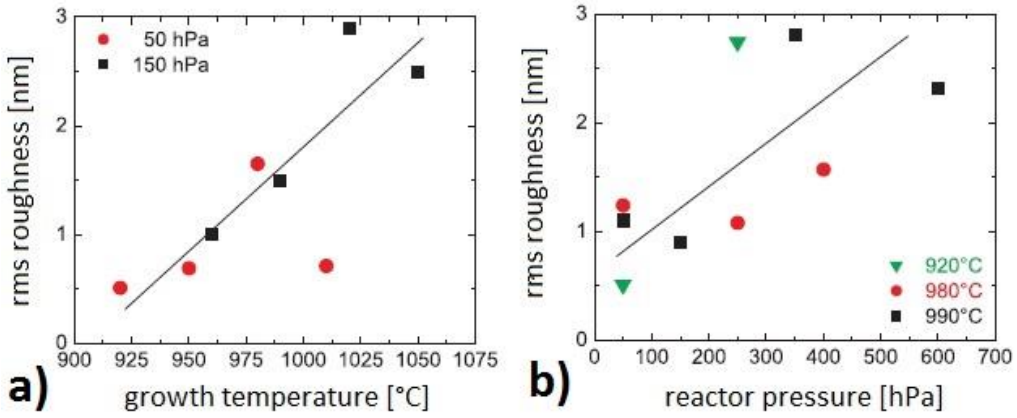

FIG. 2.4. Surface roughness of semipolar (20-21)-GaN layers as function of the a) growth temperature and b) reactor pressure for different growth temperatures [6].

variations cannot due only to the variations of the growth parameters: the mean undulation period increases also because of the simultaneous undulation bunching. The bunching of undulations has not a strict periodicity. However, the mean distance between two bunches is related to temperature through an Arrhenius-behavior. The similar influence of the growth parameters on the undulation bunching for the two semipolar (11-22)-GaN and (20-21)-GaN surfaces indicates the possible relation of the

bunching with the adatom diffusion. A comprehensive understanding of the bunching requires further investigations.
The understanding of the macroscopic observations of the morphology of the semipolar (20-21)-GaN samples requires an atomic model of the surface. First, we consider a model which neglects possible surface reconstructions. The aim of the model is to show on atomic scale that the

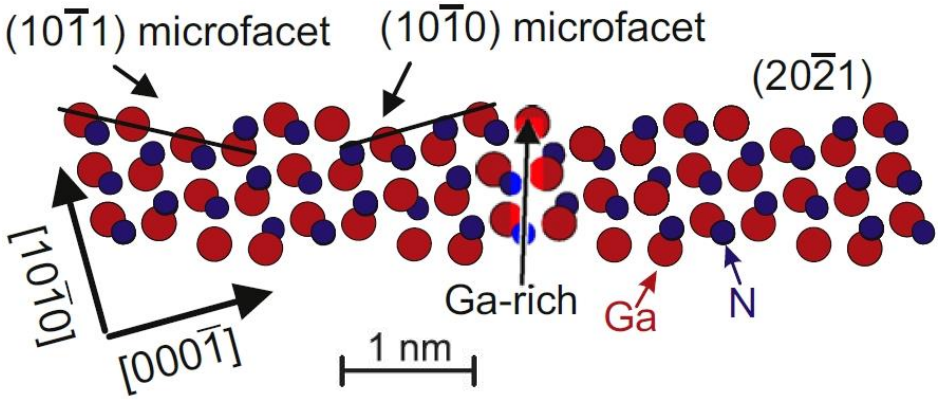

FIG. 2.5. Model of a semipolar (20-21)-GaN surface [23].

surface necessarily consists of steps. Investigations of (11-22)-surfaces with Transmission Electron Microscopy (TEM) show that the morphology undulations are related to facets of 200 nm length. In the case of (20-21)-GaN, the terraces between the steps consist probably of (10-11) and (10-10)- facets having a length of at least 1 nm (consequently they are called microfacets). Thus, along [10-1-4] the surface can be seen as alternating microfacets with a periodicity around 2 nm. Since the (20-21)-surface consists itself of undulations, it is reasonable to observe undulations in AFM images of clean samples.

2.3 Semipolar GaN substrates

At present, commercially available GaN-based electronic devices are manufactured mainly by heteroepitaxy of quantum structures on a foreign substrate like sapphire or SiC. This leads to generation of large threading dislocation density, limiting power efficiency and lifetime of the devices. The ideal solution of this problem would be the use of bulk GaN substrates for homoepitaxy. However, due to the high melting temperature, bulk GaN crystals cannot be synthesized by standard equilibrium growth methods, limiting the availability on the market [24]. Recently, InGaN/GaN high brightness LEDs and laser diodes have been demonstrated using (20-21)-plane freestanding GaN substrates [25].

High-quality nonpolar GaN substrates have been grown by Halide Vapor Phase Epitaxy (HVPE) [26]. However, because the state-of-art freestanding GaN substrates are usually sliced from a certainly bowed c-plane GaN boule grown on (0001) Al_2O_3 substrates, the tilt and twist mosaics of the initial c-plane GaN are transferred to in-plane twist. The residual mosaics are the origin of unintentional miscut of the substrate surface, which gives rise to the evolution of inclined planes, resulting in undulated surface morphology of GaN. This undulated morphology were observed also for semipolar (20-21) GaN substrates (as reported in the section 2.2). Accordingly, there remain concerns if such structural imperfections would cause inhomogeneous incorporation of In during the InGaN growth [27].

Hybride Vapor Phase Epitaxy (HVPE) is currently the technique of choice for the fabrication of high-quality and large-size native GaN substrates use for homoepitaxial growth of laser diode structures with a low density of extended defects. The high quality of HVPE grown GaN substrates has been demonstrated with benchmarking material properties in many applications, i.e. for semi-insulating and n-type GaN substrates or for semipolar and for nonpolar orientations. Moreover, HVPE is suitable for industrial use because of the relatively low growth temperatures of up to 1050 °C with the absence of high pressure. However, the wafer-by-wafer technology may reach its economic limit when such high-quality substrates are to be used for large scale production of LEDs for general lighting applications. The search for a way out led to new approaches. GaN substrate market is currently not achieved [28].

In order to overcome these problems the ammonothermal method was proposed: this method enables the growth of large diameter crystals of high crystalline quality and is a well-controlled and reproducible process performed at relatively low temperature. The growth process occurs as follows: the GaN feedstock is dissolved in supercritical ammonia in one zone of high pressure autoclave, the transported to another via convection, where crystallization on GaN seeds takes place due to supersaturation of the solution. The crystal growth proceeds in a temperature range between 500 °C and 600 °C and in a pressure range between 0.1 and 0.3 GPa. Extremely flat crystal lattice of bulk boule in GaN obtained by ammonothermal method is the biggest advantage in producing non-polar or semi-polar substrates [24]. They are not limited in length due to crystal bowing, contrary to the crystals produced by (HVPE).

2.4 Indium incorporation and critical thickness

Polar, semipolar and nonpolar wurtzite III-nitride films exhibit differences in indium incorporation. The high indium incorporation necessary in the active regions for long-wavelength light emitting devices has important consequences in terms of stress management. Managing stress in lattice-mismatched semiconductor films is essential for the successful design of bandgap-engineered devices.

Relaxation processes for c-plane films typically involve formation of V-defects and subsequent local dislocation plasticity in the case of InGaN/GaN films. For semipolar families of planes such as (11-22) and (20-21), the basal plane is inclined with respect to the growth orientation, which results in the presence of substantial shear stresses in lattice-mismatched InGaN and AlGaN films [29]. The stresses depend on the lattice misfit strain and the inclination angle of the semipolar plane. These stresses provide the driving force for formation of misfit dislocations (MDs) by basal plane glide. An example of this is illustrated in figure 2.6.

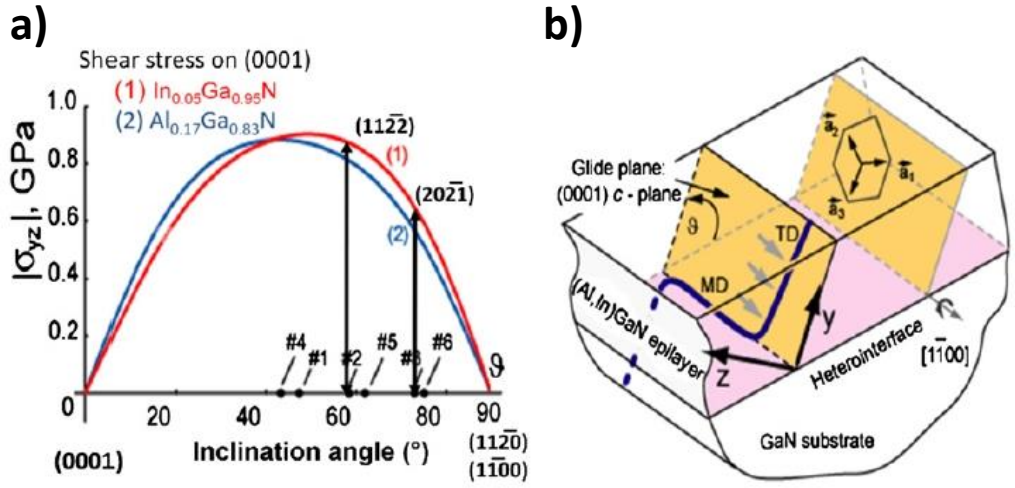

FIG. 2.6. a) Resolved shear stresses on the basal plane for compressive InGaN and tensile AlGaN films on GaN as function of inclination angle from the basal plane; b) Scheme of misfit dislocation (MD) formation by glide of a pre-existing threading dislocation (TD) for a (11-21) heterostructure [1].

The coherency limits for semiconductor film growth as a function of lattice mismatch were evaluated via the equilibrium approach of Matthews-Blakeslee where the elastic energy in a strained film is compared with the energetics of MD formation by glide. This yields a critical thickness for a film at a given strain and composition beyond which the formation of MDs is energetically favorable compared to maintaining coherency. Such an approach does not take into account the kinetics involved. In the case

of III-nitrides, the density of threading dislocations (TDs) is sufficiently high to relax the largest misfit stresses without the need for additional nucleation of dislocations. As a result, the Matthews-Blakeslee limit has been found to be an accurate lower bound for the majority of semipolar III-nitride systems.
The existence of plastic relaxation mechanisms for lattice-mismatched semipolar films has important implications for device design. Two approaches to device design are possible:

1) Design coherent devices making use of theoretical predictions and experimental demonstrations of critical thickness to design and grow heterostructures that will remain fully coherent, ensuring that there is no MD formation.
2) Design metamorphic devices in which a relaxed buffer layer can be used to tailor the lattice constant, to isolate defects from the active region of the device and even to alter the structure of the valence band.

The second approach has been successfully applied to making solar cells, transistors and light emitters based on zincblende III-V materials and has the potential for similar applications to semipolar III-nitride semiconductors [1].

For semipolar InGaN/GaN heterostructures, dislocations in the GaN substrate can propagate into the InGaN/GaN interface and glide in the basal plane to the surface. The layer relaxes along the [10-1-4] direction but remains strained along [-12-10]. As a result, the InGaN layer thickness above which misfit dislocations (MDs) and thus layer tilt occurs is referred to as the critical layer thickness. Macroscopic tilt present in a film is easily detected via symmetric x-ray diffraction (XRD) and the presence of has been confirmed by TEM. Recently, the indium incorporation efficiency and critical layer thickness for MD formation in (20-21) InGaN layers were investigated [30]. InGaN layers with an indium content between 1.7% and 16% were grown by MOVPE. The strain state of the (20-21) layers was determined from x-ray diffraction (XRD) reciprocal space maps (RSM). The indium content and layer thickness were determined from XRD symmetrical θ-2θ scans using the method of Young et al. [31]. The (20-21) layers have been classified as strained, partially relaxed and fully relaxed, according to the amount of tilt in the symmetrical RSM (figure 2.7).

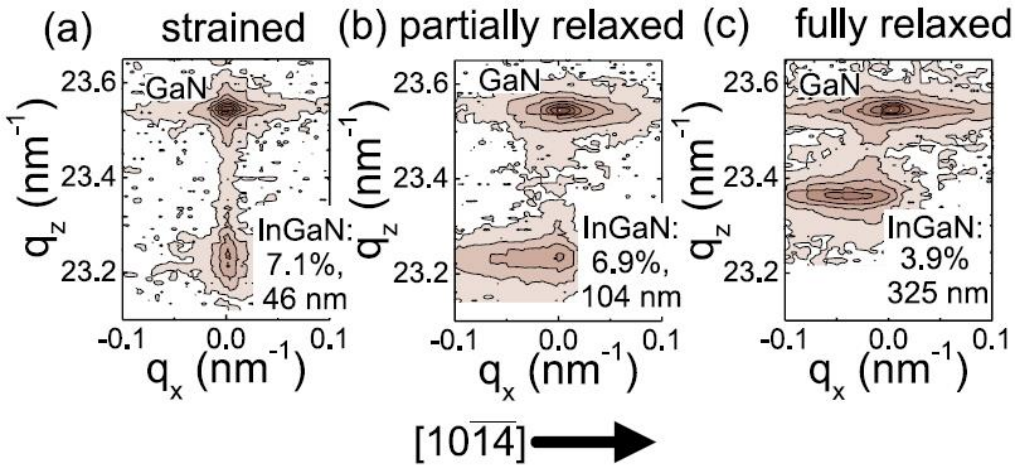

FIG. 2.7. Symmetrical (20-21) XRD RSM of a) strained, b) partially relaxed and c) fully relaxed InGaN layers [30].

Partially relaxed layers exhibit a negligible tilt relative to the GaN substrate and have a thickness which might be very close to the critical thickness. The critical thickness value between 55 nm and 110 nm found by Hardy et al. [32] for an indium content of 6% agrees with the observations of Ploch et al. [30]. The critical layer thickness exhibits a behavior as predicted by the Matthews and Blakeslee model, with some deviations. A reduced indium incorporation efficiency was found in comparison to (0001) oriented InGaN layers at growth temperature of 725 °C. The reduced indium incorporation efficiency on (2021) layers in comparison to (0001) layers disagrees with observations made for NH_3 MBE growth, where a higher indium incorporation in (20-21) layers in the growth temperature range between 575 °C and 650 °C was found [33].
It seems that a general statement on the indium incorporation efficiency cannot be made. However, the influence of growth parameters on indium incorporation efficiency remains under investigation.

2.5 Semipolar InGaN LEDs

Group-III nitride based laser diodes and light emitting devices in the visible spectrum employ InGaN quantum wells as active regions.
The standard design for a LED structure is illustrated in figure 2.8. For the LED structure in figure 2.8a, the active region is composed by a InGaN layer surrounded by InGaN barriers. A p-type AlGaN:Mg electron blocking layer (EBL) avoids that electrons diffuse in the p-GaN side, improving the efficiency of the device. This design was developed for LEDs grown on a polar substrate, as well as for semipolar substrates.

However, in order to evaluate the polarization fields, the LED structure must be kept as simple as possible, because every heterointerface gives rise to additional fields. Therefore, a second kind of LED structure without the EBL and instead with an InGaN multiple quantum well (MQW) was employed (figure 2.8b). Moreover, the presence of a MQW allows a greater spatial extension of the active region.

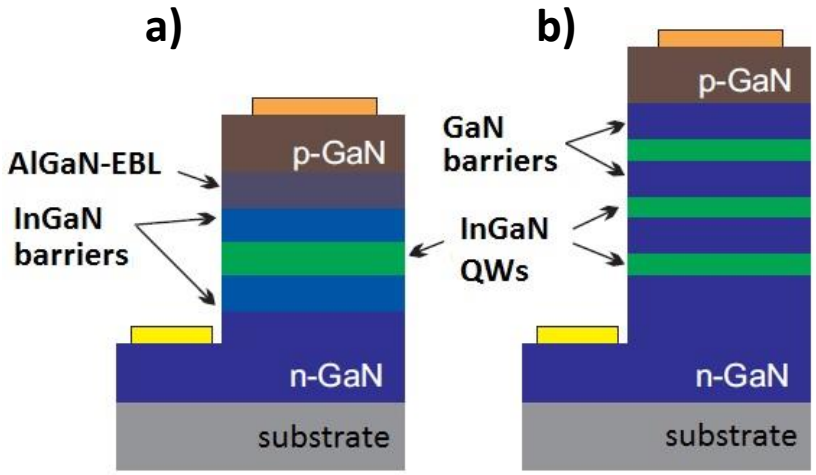

FIG. 2.8. Epitaxial structure of two standard LEDs; a) single quantum well structure with electron blocking layer and b) multiple quantum well structure without electron blocking layer [34].

The realization of efficient light emitting devices becomes more difficult with an increasing indium content in the layers. First, the QCSE becomes stronger at higher wavelengths and, second, the incorporation of more indium leads to higher fluctuations of the indium composition in the active region. This fact results in an increase of the line width with increasing emission wavelength in the emission spectra of LEDs.
The emission energy of a QW is mainly determined by the energy gap of the material and by the barrier width, but it can also be affected by the measurement conditions like the sample temperature. The interdependence of indium content, strain and quantum confined stark effect (QCSE) on the emission energy can be very complex. A proper estimation of the different effects is only possible by calculating the QW band structure, taking into account polarization fields and strain and solving the Schrödinger-Poisson equation.

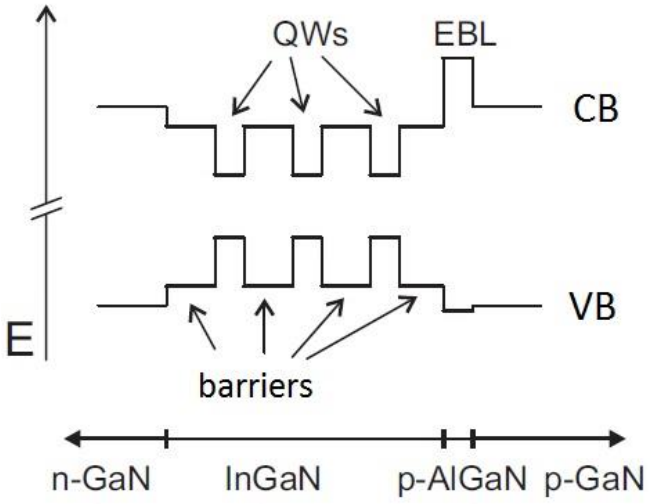

FIG. 2.9. Schematic band structure of the active region of a LED [34].

The emission wavelengths of MOVPE grown InGaN QWs were investigated by Wernicke et al. [35] for different crystal orientations with electro luminescence (EL) and photo luminescence (PL). The indium incorporation was estimated by comparison of the emission energies to kp-theory calculations. The normalized emission spectra for InGaN QWs deposited on differently oriented substrates are showed in figure 2.6.

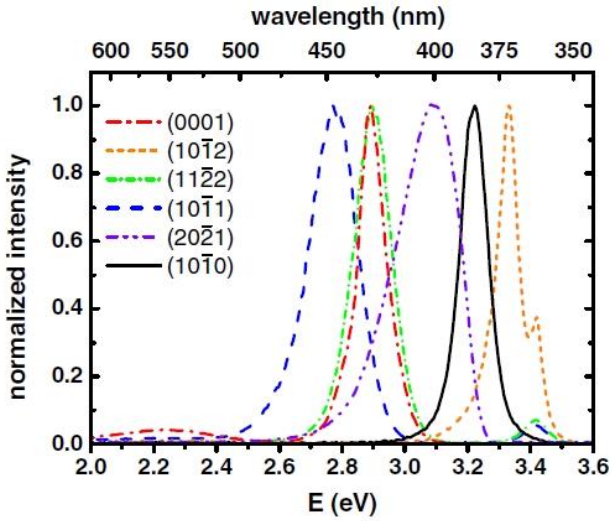

FIG. 2.10. Normalized room-temperature PL and EL emission spectra for c-plane, semipolar and nonpolar InGaN QWs grown at 750 °C [35].

A large variation of the emission energy of almost 600 meV for QWs that were all grown under the same conditions can be observed. A strong variation of the emission energy was observed for InGaN QWs grown at

the same temperature of at 750 °C on differently oriented substrates. A clear hierarchy was identified:

$$(10\text{-}11) < (11\text{-}22) = (0001) < (20\text{-}21) < (10\text{-}10) < (10\text{-}12)$$

The comparison between kp-theory and experimental results allow to separate the effect of indium content on the effects of QCSE and strain. The analyses yielded similar indium incorporation efficiencies for (0001), (20-21), (10-12) and (10-10) surfaces. The differences in the emission energy for these orientations can be mainly attributed to the QCSE and the effect of anisotropic strain.

Chapter 3
Surface-analytic experimental techniques

In this chapter, we give an overview on the experimental techniques (listed in table 3.1) used to investigate our semipolar (20-21) InGaN samples. First, we briefly describe the context in which the surface becomes a fundamental physical property and, second, we present the main characteristics of each used experimental surface technique.
The surface of a solid can be very complex. Surface analysis means, in the simplest sense, that the elemental composition of the outermost atom layers of a solid is required. Having found that, there will be immediate requests for detailed knowledge of the chemical binding state, surface reconstructions, surface homogeneity and state of adsorbates. Each of the many surface analysis techniques approaches one or more different aspects better than the others so that, in principle, each has a particular advantage.

Physical property	Experimental technique
Symmetry and periodicity	Low Energy Electron Diffraction (LEED)
Morphology	Atomic Force Microscopy (AFM)
Atomic structure	Scanning Tunneling Microscopy (STM)
Chemical properties and bonds	X-ray Photoemission Spectroscopy (XPS)
Optical Properties	Surface Photovoltage Spectroscopy (SPS)

TAB. 3.1. Experimental techniques used for the investigation of the semipolar (20-21) InGaN samples in this thesis.

3.1 Surface physics

Semiconductor physics cannot be separated from the concept of surface physics. First, the growth of semiconductor materials is realized with techniques which consist in appropriate manipulations of a variety of kinetic processes and chemical reactions which occur at the surface (see section 1.6). Second, the effect of the surface becomes increasingly stronger as the process of miniaturization in the semiconductor technology proceeds. Thus, the study of the surface becomes a fundamental issue, not

only for topics of fundamental physics like the transition into the regime of quantum physics, but also for technological purposes. In this sense, the semiconductor research in the last decades has been involved also with topics such as the development of suitable surface preparation methods and the material handling in vacuum conditions.

3.1.1 General considerations

The concept of surface physics is important not only in connection with special experimental tools, but also for certain physical systems. In many theoretical models in the classic solid state physics, the properties of the surface atoms are neglected because their number is several orders of magnitude lower than the number of bulk atoms. However, this condition is no longer satisfied in solid thin films. When probes which are used "strongly" interact with solid matter and penetrate only a couple of Angstroms into the solid, the models of surface physics have to be applied. The same is true for spectroscopic techniques where the particles detected outside the surface originate from excitation processes close to the surface.

A solid interface is defined as a small number of atomic layers that separate two solids in intimate contact with one another, where the properties differ significantly from those of the bulk material it separates. The surface of a solid is a particularly type of interface, at which the solid is in contact with the surrounding world, i.e., the atmosphere or, in the ideal case, the vacuum [21]. The term morphology refers to the macroscopic form or shape of a surface, whereas the structure, on the other hand, denotes the detailed geometrical arrangement of atoms. The distinction between the two terms, however, is sometimes not so clear, even in the case of clean and well-defined surfaces. What we consider as morphology depends on the resolution of the techniques used for its observation. Furthermore, the atomistic structure may often determine, or at least have a significant influence on, the morphology of a surface. It is thus necessary to consider both aspects in the surface analysis of a material.

3.1.2 Ultra high vacuum (UHV)

The word vacuum is used to describe a wide range of conditions. At one extreme, it refers to nearly complete emptiness, i.e. a space in which air and other gases are absent. At the other extreme, vacuum is any gas pressure less than a prevailing pressure in an environment. In each case, the basic property involved is the gas density. Ultra high vacuum (UHV) is a physical condition which requires a pressure of around 10^{-9} mbar. Furthermore,

UHV is not only determined by a pressure condition, but also by a precise chemical condition: air is primarily a nitrogen ambient, whereas UHV is instead a hydrogen ambient. The presence of other minor gases depends on the used vacuum pumps.

The vacuum can be produced by different methods, like mechanical displacement of gases from an enclosed space, chemical reactions which produce solid residues, physical adsorbtion or gas ionization [36]. To produce UHV in a chamber, the evacuation process must start at atmospheric pressure and a sequence of at least two different pumping devices is used. Usually, a rough vacuum level is produce by mechanical pumps and the high vacuum level is developed by diffusion pumps or ion-gettering pumps. The ion getter pumps are mostly used for pressures lower than 10^{-9} mbar and remain the cleanest and most efficient method to achieve ultra high vacuum (UHV). The pump captures gases by converting them into solid compounds and binding them inside the pump. Furthermore, ion getter pump operate free of vibrations and agitations at very low power consumption. The ion getter pumps are an integral part of scientific apparatus as particle accelerators, space simulations, mass spectrometers and development and production of semiconductor devices.

There are two reasons why electron spectrometers used in surface analysis must operate under vacuum conditions:

1) The mean free path of the emitted electrons should be much greater than the dimensions of the spectrometer. That means that the electrons should meet as few gas molecules as possible on their way to the analyser so they are not scattered and thereby lost.
2) Surface contamination from whatever source should be avoided because every small amount of contaminant can affect the analysis.

The sample treatment in UHV requires the preparation of a clean surface. In this context, clean surface is defined as the state of the surface in which the experimental techniques (like XPS and AES) cannot detect characteristic spectral features of impurity elements. The simplest cleaning technique is heat treatment, generally a few hundred Celsius degree below the melting point of the material. The problem is to maintain the cleanliness of the sample on cooling to room temperature, since the temperature will pass through ranges in which impurities segregate quickly to the surface. Another technique used to remove impurities is the ion bombardment, typically with a beam of Ar ions of energy around keV. In some applications and analyses the residual low level of contamination may

be acceptable, while in other applications it is necessary to use a combination between more cleaning techniques [37].

3.1.3 Surface preparation

The preparation of semiconductor devices often requires processing in several different atmospheres and, hence, sample transfer between those. During transfer, surface oxidation and other contamination are likely to occur. A minimization of surface contamination is crucial for subsequent device processing as surface defects can govern epitaxial growth and may lead to the formation of bulk defects that cannot be overgrown without substantial effort. This may also lead to deteriorated electronic properties of interfaces. Therefore, the availability of an effective cleaning process of the semiconductor surface after transfer is of crucial importance. Besides oxide formation, the major contaminant on semiconductor surface is residual carbon.
For III-nitride alloys, several cleaning techniques has been tested. It has been demonstrated that thermal annealing, i.e. heat treatment, strongly improves the cleanliness of samples after dry nitrogen transfer and related exposure to residual oxygen. Moreover, plasma assisted cleaning is shown to successfully further remove carbon contaminations [38].

3.2 Electron spectroscopy

Chemical analysis of solid materials with electron spectroscopy is based on energy analysis of secondary electrons that are emitted as a result of excitation by photons, electrons or ions. The main features of the electron spectroscopy techniques are:

1) Detection of all elements except hydrogen and helium
2) Detection of chemical bonding states
3) Information depth in the nanometer range

The reason for the surface specificity of electron spectroscopy is the small information depth of typically some nanometers that is determined by the elastic mean free path of electrons between typically 40 eV and 2500 eV. The most important methods that are employed in commercial surface analytical instruments are X-ray Photoelectron Spectroscopy (XPS) and Auger Electron Spectroscopy (AES). The two techniques are comparable in their surface sensitivity, however peak are analysis in XPS is more accurate than Auger peak to peak height in AES.

The most important part of an electron spectrometer is the electron energy analyzer. At present, all commercial photo-electron spectrometers are equipped with a concentric hermispherical analyzer (CHA). The CHA consists of two concentric hemispheres and the outer hemisphere is put on a negative potential against the inner sphere: the mean radius describes an equipotential plane that connects entrance and exit slits. The main purpose of the input lens is retardation of the electrons to reduce their energy before they enter the analyzer. This reduced and constant energy is called pass energy. A CHA spectrometer is shown in figure 3.2.
CHA spectrometers can be operated in two different modes, the constant retard mode (CRR), where $\Delta E/E$ is constant, or the constant analyzer mode (CAT), where ΔE is constant. Whereas the CRR mode is generally used in AES, the CAT mode is exclusively used in XPS [39].

3.2.1 X-ray photoelectron spectroscopy (XPS)

XPS is a quantitative spectroscopic technique that measures composition, chemical state and electronic state of the elements that exist within a solid surface. The Photoelectron emission can be imagined as a three-stage process:

1) X-ray interact with the electrons in the atomic shell
2) Photoelectrons are generated and part of these move to the surface after being subject to various scattering processes
3) Electrons reaching the surface are emitted in the vacuum

The kinetic energy of a photoelectron is schematically derived from the energy level scheme shown in figure 3.1. An X-ray with energy $h\upsilon$ generated a vacancy in a core electron level with binding energy E_b. The emitted photoelectron has to overcome the work function of the sample Φ_S. Thus, with reference to the Fermi energy E_F, the energy measured by the analyzer is

$$\begin{aligned} E_{kin} &= h\upsilon - E_b - \Phi_S - (\Phi_A - \Phi_S) = \\ &= h\upsilon - E_b - \Phi_A \end{aligned}$$

Because the sample work function is constant and the photoelectron energy is known, the measured photoelectron spectrum is a direct indication of the binding energies of the different atomic electron levels.

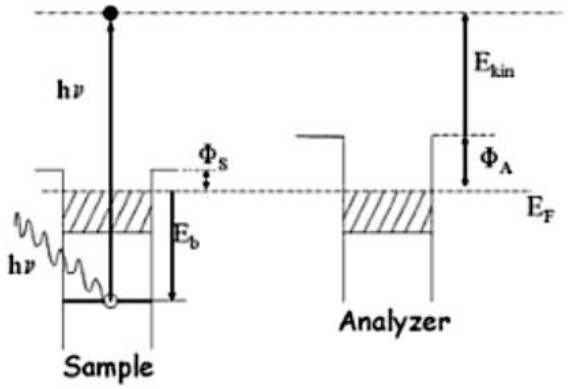

FIG. 3.1. Scheme of the relevant energy terms in XPS of solid surfaces [39].

A scheme of a typical XPS experimental setup is shown in figure 3.2. The most common X-ray sources used in XPS are equipped with Mg or Al anodes, which exhibit a characteristic K_α radiation of 1253.6 eV and 1486.6 eV, respectively. A thin Al foil of about 2 μm thickness is placed at the exit of the X-rays to shield the sample from stray electrons, from contamination and from the heat. For efficient irradiation, usual sources are operated at (0.5÷1) kW power, at (5÷15) keV anode voltage.

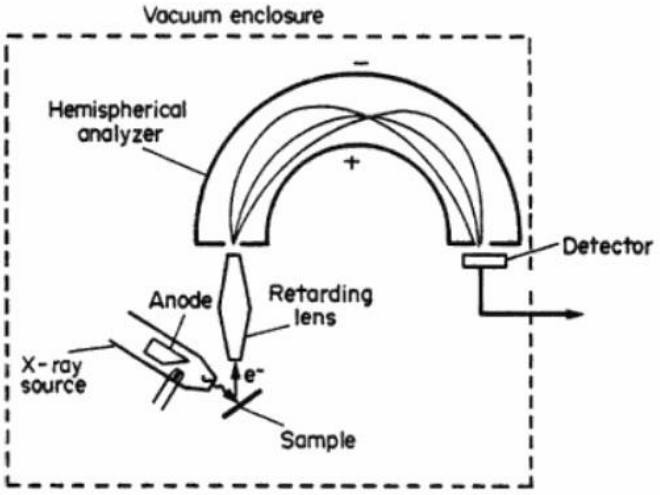

FIG. 3.2. Scheme of a typical XPS experimental setup [39].

The necessity of forced water cooling to remove the heat from the anode also implies that the anode block must be of high heat conductance, which in turn means fabrication of the block and the integral water tubes from copper. Thus, the anode material itself is normally deposited on the copper block as a thick film, typically 10 μm, representing a compromise between being thick enough to exclude copper L_α radiation and thin enough to

allow adequate heat transfer [37]. Most of the commercially available X-ray sources have two anode surfaces and it is possible, by simple external switching, to choose one of them. There are two reasons why it is desirable to have a double-anode facility:

1) The two characteristic emission radiations have two different line width allowing two different resolutions

2) The XPS spectrum, both photoelectron and Auger peaks appear, with possible interferences. Since Auger energies are fixed, a change in the X-ray line energy will resolve possible interferences.

For identification of possible differences in chemical states of elements, in XPS it is necessary to apply the same absolute energy resolution to any peak in the spectrum, i.e. at any kinetic energy. It is standard practice to retard the kinetic energies of the electrons either to a chosen analyzer energy, the so-called pass energy. In either case the pass energy is kept fixed during the acquisition of any spectrum. Retardation enables the same absolute resolution to be obtained for a lower relative resolution.

3.2.2 Interpretation of XPS spectra

The XPS technique counts the electron ejected from a sample surface when it is irradiated by X-rays. A spectrum representing the number of electrons recorded at a sequence of energies includes both a contribution from a background signal and also resonance peaks characteristic of the bound states of the electrons in the surface atoms. The resonant peaks above the background are the significant features in typical XPS spectrum, as shown in figure 3.5.
Any change in the bonding state of an atom gives rise to changes in the observed spectral characteristics: binding energy, peak width and shape, valence band changes and sometimes bonding satellites. Chemical bonding in a compound usually causes a change of the binding energy as compared to bonding in the pure element which is called chemical shift. Ignoring final-state effects, the chemical shift can be explained by the effective charge potential change on an atom. For example, when an atom is bonded to another one with higher electronegativity, a charge transfer to the latter occurs and the effective charge of the former becomes positive, thus increasing the binding energy. In practice, references to standard spectra of compound are used to interpret measured chemical shifts [39]. The chemical shifts seen in XPS data are a valuable source of information about

the sample. For example, semiconductor surfaces are often covered with an oxide layer: this can be observed in the XPS spectrum as separation between elemental and oxide peak for a given element.

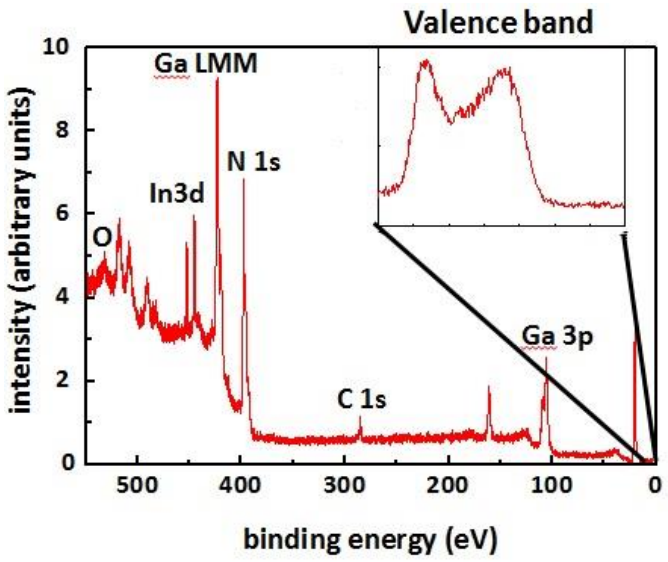

FIG. 3.3. XPS spectrum of a semipolar InGaN sample (own measurement). One can identify the core level peaks N 1s, Ga 3p, In 3d, the surface contaminants C 1s and O and the Ga LMM Auger peak. An inset of the valence band is also illustrated.

The underlying assumption when quantifying XPS spectra is that the number of electrons recorded is proportional to the number of atoms in a given state. XPS spectra are, for the most part, quantified in terms of peak intensities and peak positions. The peak intensities measure how much of a material is at the surface, while the peak positions indicate the elemental and chemical composition [40]. Other values, such as the full width at half maximum are useful indicators of chemical state changes. Broadening of a peak may indicate:

1) Change in the number of chemical bonds
2) Change in the sample condition
3) Differential charging of the surface

Not all the electrons emitted from the sample are recorded by the instrument. The efficiency with which emitted electrons are recorded depends on the kinetic energy of the electrons, which in turn depends on the operating mode of the instrument. So, the best way to compare XPS intensities is via percentage atomic concentrations, i.e. the ratios of the intensity to the total intensity of electrons in the measurement. Should the

experimental conditions change between measurements, for example the X-ray gun power output, then the peak intensities will change in an absolute sense, but they will remain constant in relative terms.
The first issue involved with quantifying XPS spectra is identifying those electrons belonging to a given transition. The standard approach is to define an approximation to the background signal. A variety of background algorithms are used to measure the peak. However, none of these algorithms is favored, so that the arbitrariness of the choice represents a source for uncertainty. Peak areas computed from the background subtracted data form the basis for most elemental quantification results form XPS. Relative sensitivity factors of photoelectric peaks are often tabulated and used routinely to scale the measured intensities as part of the atomic concentration calculation. An accuracy of 10% is typically quoted for routinely performed XPS atomic concentrations.

3.2.3 Auger Electron Spectroscopy (AES)

In a typical AES experiment, the sample is irradiated with a focused beam of primary electrons of sufficiently high energy, (1÷20) keV, from the electron gun which penetrate the sample up to a range of the order of (0.1÷1) μm. Auger electrons possess characteristic energies which are well defined by the involved electron levels of the analyzed element [39]. Auger electron emission is imagined as a three-stage process which involves three electron levels:

1) An atom of the sample is ionized by electron impact.
2) The resulting vacancy in a core electron shell will be filled by an electron from a higher level.
3) The excess energy will cause either emission of a characteristic X-ray or emission of another electron, called Auger electron, which leaves the atom with a characteristic energy.

The measured Auger electron energy is given by the difference between the binding energies of the involved electron levels, i.e. referring to figure 3.4 one has

$$E_{WXY} = E_W - E_X - E_Y - \Phi_A$$

By calibration of the analyzer using the elastic peak (with well-defined energy usually at 2 keV), the work function Φ_A is removed from this equation. Reference samples for which standard kinetic energies are available help to establish a correct energy scale.

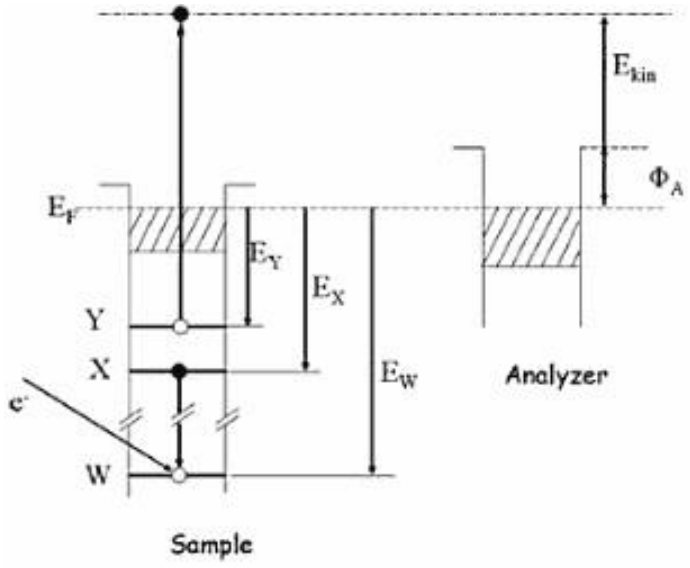

FIG. 3.4. Schematic energy diagram for Auger electron excitation, emission and measurement, involving the three electron levels W, X, Y. The hatched areas indicate the valence band [39].

The most prominent Auger peaks are:

- KLL transitions for elements with atomic number Z = (3 ÷ 14)
- LMM transitions for elements with atomic number Z = (14÷ 40)
- MNN transitions for heavier elements

Today, practically all AES instruments are operating in the digital (pulse counting) mode which directly yields the intensity as function of the kinetic energy. Frequently, the first derivative of the direct spectra is measured: in analog equipment with retarding grids, it is directly obtained by detection of the second harmonic of the modulation frequency by a lock-in amplifier. Differentiation provides an apparent automatic background subtraction and the intensity is measured as the Auger peak-to-peak height.
The most common limitations encountered with AES are related to charging effects in non-conducting samples. Charging results when the number of secondary electrons leaving the sample is different from the number of incident electrons, giving rise to a net positive or negative electric charge at the surface. The surface charges distort the measured Auger peaks. Several processes have been developed to contrast the issue of charging, though none of them is ideal and still make quantification of AES data difficult.

3.3 Scanning probe microscopy (SPM)

The scanning probe microscopy is one of the modern research techniques that allow to investigate the morphology and the local properties of solid surfaces with high spatial resolution. Currently, every research in the field of surface physics and thin-film technologies applies the SPM techniques. After considering the common features inherent to various probe microscopes, the special characteristics of the two most used techniques, atomic force microscopy (AFM) and scanning tunneling microscopy (STM), are considered.

3.3.1 Working principle of SPM

The surface analysis by scanning probe microscopes is performed using specially prepared tips in the form of needles. The size of the working part of such tips (the apex) is around few nanometers. Various type of interaction between tip and surface are exploited in different types of probe microscopes.
The interaction between tip and surface depends on a parameter P that is used in a feedback system (FS) to control the distance between tip and surface. A block diagram of the feedback system is illustrated in figure 3.3. The feedback system is based on a piezo transducer (PT) that allows restoring the preset value of the distance in real time with high accuracy.

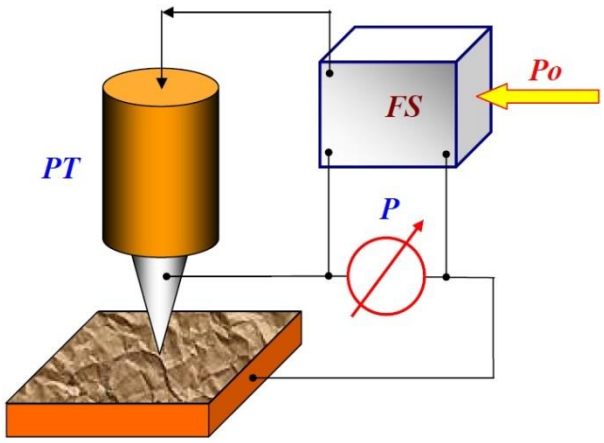

FIG. 3.3. Block diagram of the feedback system (FS) in a SPM microscope [41].

So, when the tip is moved over the sample the signal fed to the transducer is proportional to the local departure of the sample surface from an ideal

plane. This makes possible to use this signal to map the surface topography and obtain an SPM image [41]. During scanning the tip first moves above the sample along a certain line, thus the value of the signal, proportional to the height value in the surface topography, is recorded in the computer memory. Then the tip comes back to the initial point and steps to the next scanning line: the process repeats again. The information collected is stored as a two-dimensional matrix of integer numbers, which physical meaning depending on the kind of interaction measured during scanning. Each element of the matrix corresponds to a point of the surface. Visualization of SPM frame is done by computer graphics. In addition, various ways of pixel brightening corresponding to various height of the surface.

Beside these maps of tip-sample interaction over the scanning area, a different type of information can be retrieved by SPM. For example, on a single point of the surface it can be collected the dependence of the tunneling current on the applied voltage. SPM images, alongside with the helpful information, contain also a lot of secondary information affecting the data and appearing as image distortions. Possible distortion could be due to scanner imperfections, tip-sample contact instability, rough surfaces, external vibration noise [41].

The probe microscope scanners or transducers are made of piezoceramic materials. Piezoceramic is polarized polycrystalline material obtained by powder sintering from crystal ferroelectrics. The polarization is performed by heating up the material above the Curie temperature and subsequently cooling down in a strong electric field. After cooling below the Curie temperature, piezoceramic retains the induced polarization and gets the ability to change its sizes. Assembly of three tubular piezoelements in one unit, called tripod, allows to produce precise movements in three mutually perpendicular directions. An important technical requirement of scanning probe microscopy (and in general thin films surface analytical techniques) is the precision of movements of tip and sample. Requirements of good insulation from external vibrations and necessity of working under vacuum imposes restrictions on application of mechanical devices for tip and sample movements. In this respect, devices based on piezoelectric converters such as step-by-step piezoelectric motors became widely used.

3.3.2 Atomic force microscopy (AFM)

The AFM working principle is the measurement of the interactive force between tip and sample using special probes made by an elastic cantilever with a sharp tip on the end. The force applied to the tip by the surface atoms results in bending of the cantilever: measuring the cantilever

deflection it is possible to evaluate the tip-surface interaction. The small deflections of the elastic cantilever are recorded by means of an optical system (figure 3.4). The system is aligned so that the light beam emitted by a diode laser is focused on the cantilever and the reflected beam hits the center of a photodetector. Four section split photodiodes are used as position-sensitive photodetectors.

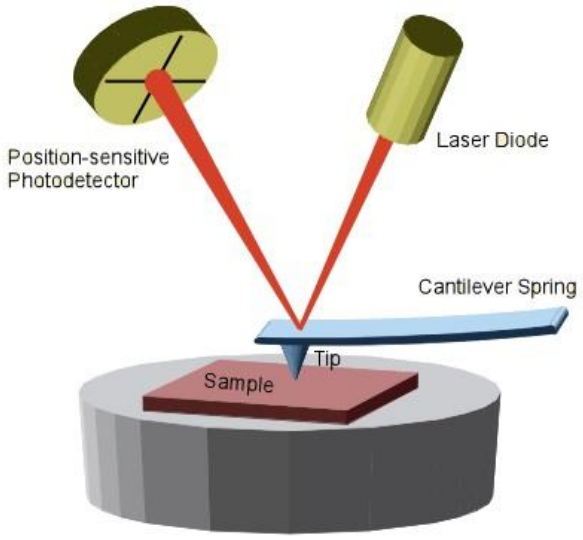

FIG. 3.4. Scheme of the optical system able to detect the cantilever bending [42].

The operation methods of an AFM microscope can be split in two groups:

- In contact mode the tip apex is in direct contact with the surface. The force acting between tip and sample is counterbalanced by the elastic force produced by the deflected cantilever. The feedback system can provide either a constant value of the cantilever bend (constant force mode) or a constant average distance between tip and sample (constant height mode).

- In the so-called semi-contact mode, forced cantilever oscillations are excited near a resonance frequency. During scanning the changes of amplitude and phase of cantilever oscillations are recorded. So, two types of AFM images are acquired simultaneously:

    - The surface topography obtained at constant amplitude
    - The corresponding distribution of phase contrast

The cantilever is approached to the surface so that in the lower semi-oscillation the tip gets in contact with the sample surface, however, the characteristic features of this mode are similar to the features of a contactless mode.

The interactive forces measured by AFM can be explained by the considering the van der Waals forces. The potential energy for two atoms,

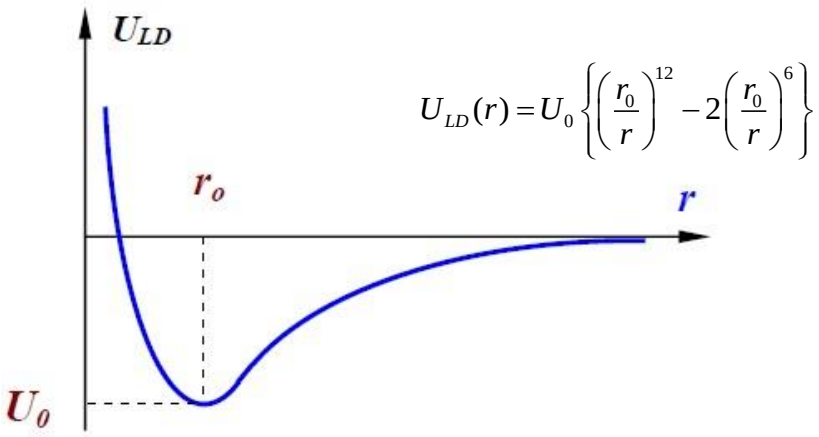

FIG. 3.5. Qualitative form of the Lennard-Jones potential. r_0 is the equilibrium distance between atoms [41].

located a distance r from each other, is approximated by the Lennard-Jones potential (showed in figure 3.5). The first term describes the long-distance attraction caused basically by a dipole-dipole interaction and the second term takes into account the short range repulsion due to the Pauli exclusion principle.

3.3.3 Scanning tunneling microscopy (STM)

Conventional STM is based on the control of the tunneling current through the potential barrier between the surface to be investigated and the probing metal tip. As the distance between tip and surface is reduced to a few atomic diameters, a small bias voltage applied between tip and surface will generate a tunneling current. The main difference between STM and other microscopies is that there is no need for lenses and special light; instead the bound electrons already existing in the sample under investigation serve as the exclusive source of radiation.

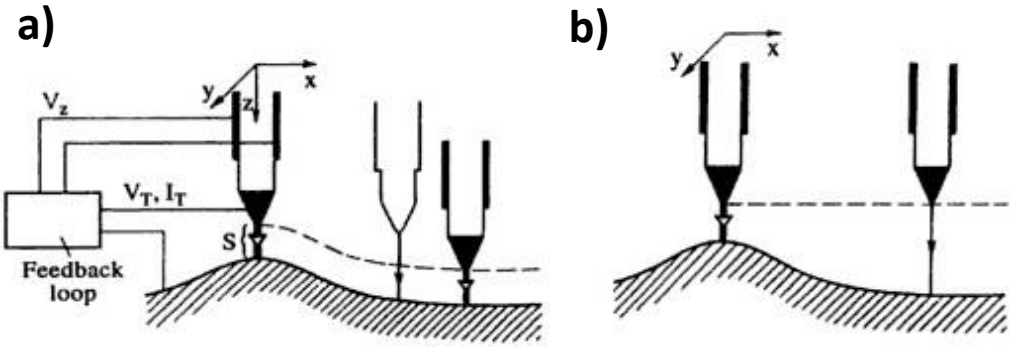

FIG. 3.6. Schematic view of the two modes of operation in STM: a) constant-current mode and b) constant-height mode [43].

As shown in figure 3.6, the STM can be performed in two modes:

1) Constant-current mode means that the tunneling current is maintained at a preset value by the feedback system, while the tip-surface separation is induced from the measurement of the bias voltage. It is suitable for surfaces which are not atomically flat.

2) Constant-height mode means that the bias voltage is kept constant and the tunneling current is monitored. This mode allows for much faster imaging of atomically flat surfaces: this enables to study dynamic processes on surfaces and minimizes the distortion due to piezoelectric creep and thermal drifts.

In any case, the exponential dependency between current and tip-sample separation is used to map the sample's surface topography. The constant topographs can be interpreted as planes of constant electronic density of states above the sample: one can relate such image to the real surface topography insofar as the spatial distribution of the electron concentration is related to the crystal structure of the surface atoms. Atomically resolved STM images hence do not show atoms but enhanced electron concentration in the vicinity of the atomic sites [44].

An important feature of STM is the possibility to perform local tunneling spectroscopy. To this end, the tunneling current is measured as a function of gap voltage at a fixed tip position. The feedback loop is opened to keep the tip at a constant distance and the bias is ramped stepwise in the range of interest. This technique allows to record IV curves in any point of a surface and is called scanning tunneling spectroscopy (STS). Usually, the resistance R_S of samples studied in STM is much less than the tunneling

contact resistance R_t, which can be around 10^8 Ω. The equivalent scheme of a tunneling contact is showed in figure 3.7.

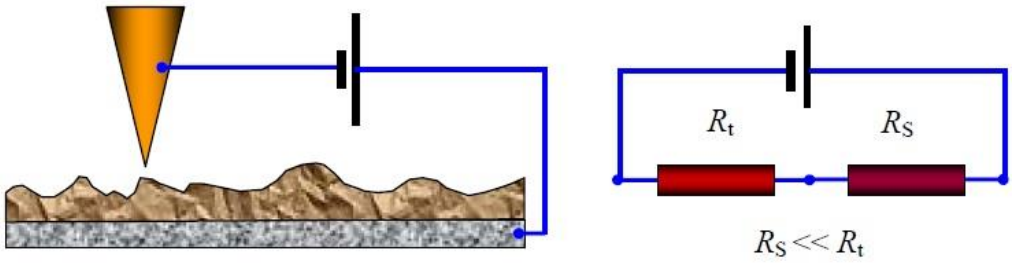

FIG. 3.7. Equivalent scheme of the tunneling contact realized in the STS technique [41].

Mainly electron with energies near to Fermi level participate in the tunneling current:

- During forward bias the electrons are tunneling from the filled states in the conduction band of the tip to the free states in the conduction band of the samples.
- During reverse bias the electrons are tunneling from the sample to the tip.

The IV curve essentially depends on the electron density of states in the sample. However, the presence of an energy gap and impurity levels in semiconductor materials makes the IV curve of a metal-semiconductor tunneling contact strongly nonlinear. Essential contributions to the tunneling current is made also by surface states and energy levels due to adsorbed atoms: this complicates the interpretation of tunneling spectra.

Some advantages of STS are the big variability of the tip-sample separation and the possibility of examination in ultra high vacuum enviroments. However, STS still suffers from the unknown contribution of the probe tip. This can lead to non-reproducibility of data resulting from tip instabilities, tip composition or structural dependencies [41]. In order to understand the possible influence of these factors, it is useful to compare the results obtained with STS with other spectroscopic techniques.

3.4 Surface Photovoltage Spectroscopy (SPS)

Surface Photovoltage Spectroscopy (SPS) is a well-established contactless and non-destructive technique for the characterization of semiconductors,

which relies on analyzing illumination-induced changes in the surface voltage. In addition, they can be performed *in situ* and *ex situ*, at any reasonable temperature and at any ambient [45]. The possibility of obtaining a detailed picture of the electronic structure of semiconductors makes (SPS) a powerful technique.

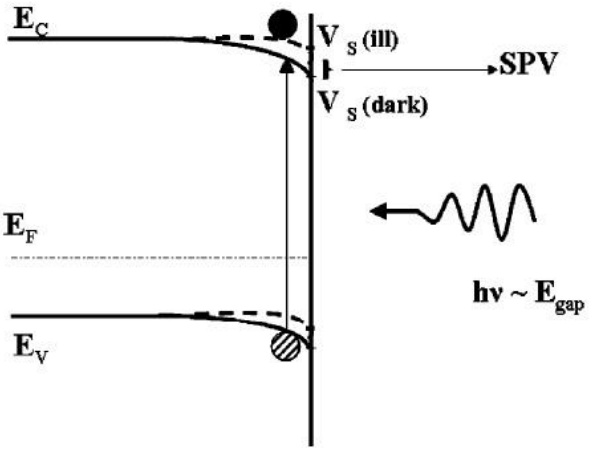

FIG. 3.8. Schematic band diagram of p-type semiconductor surface in dark and under illumination [46].

The surface potential V_s is defined as the energy difference between the bottom of the conduction band at the surface and in the bulk. As illustrated in figure 3.8, the SPV is defined as the light induced variation of the surface potential [46]:

$$SPV = V_s(ill) - V_s(dark)$$

In SPV measurements, the surface potential is a built-in potential rather than an external potential: it cannot be measured simply with some form of voltmeter. Moreover, in the case of a free surface the application of any contact to indirect electrical measurements of the built-in voltage invariably will alter the surface properties and hence the quantity under measurement. Consequently, many elaborate techniques for measuring the surface potential without applying a direct electrical contact have emerged. A possible approach is based on a metal-insulator-semiconductor (MIS) structure. The SPV signal is obtained by measuring the photoinduced external voltage change between the MIS capacitor terminals. This approach is applicable to the study of a free semiconductor surface by placing a static metallic grid in proximity to the sample, with the air or

vacuum gap functioning as the insulator, and using chopped illumination in conjunction with lock-in detection.
The first elementary application of SPS is the determination of the bandgap of a semiconductor. The large increase in absorption coefficient near the bandgap energy brings about a significant change of the SPV signal. In particular:

- When photons with energy larger than the bandgap hit the semiconductor surface, electron-hole pairs are generated and collected by the surface barrier and the surface potential is consequently reduced.

- When the photon energy equals the bandgap, the resulting SPV signal significantly increases. This variation constitutes the most significant feature in the SPS spectrum.

- When photons with energy below the bandgap hit the semiconductor surface, two different cases must be considered. It must be considered that the surface barrier is sensitive to surface states. If the energy is able to promote an optical transition from defect level to conduction band, the surface band bending increases, i.e. the SPV signal increases. On the contrary, for transitions from the valence band to defect level, the SPV signal decreases.

Detailed comparisons between SPV and absorption spectra reveal that the two are often similar but never identical. The sensitivity of the SPS in the detection of bulk defect states is similar to the sensitivity of optical absorption spectroscopy, while SPS is more sensitive for surface states [17]. As opposed to transmission spectroscopy, SPS does not require light collection and therefore can be performed on arbitrarily thick samples. It is also inherently insensitive to reflection and scattering, thus useful for heterostructures and nanocrystallites.
A second important application of SPS is the defect state characterization. Because photons of sufficient energy may excite charge carriers from a surface state to a band, or vice versa, one expects a knee in the SPV spectrum whenever the photon energy exceeds the threshold energy of a certain transition. In heterostructures, the interpretation of the slope sign of the spectrum knees is more complicated because the direction of the band bending is not determined solely by depletion or accumulation and because overlayers cause a reduction in SPV signal via simple absorption.

3.5 Low energy electron diffraction (LEED)

Low-energy electron diffraction (LEED) is a powerful method for determining the geometric structure of solid surfaces. It is similar to x-ray diffraction (XRD) in the type of information that it provides, however, instead of X-rays a beam of electrons is used. The incident electrons must be in the energy range (20 ÷ 200) eV, so they correspond to waves with wavelength comparable with interatomic distances (0.8 ÷ 2.7 Å).

The incident electrons will be scattered by the surface atoms, i.e. regions of high localized electron density, and they interfere constructively like waves. The diffracted electrons are observed as spots on a fluorescent screen.

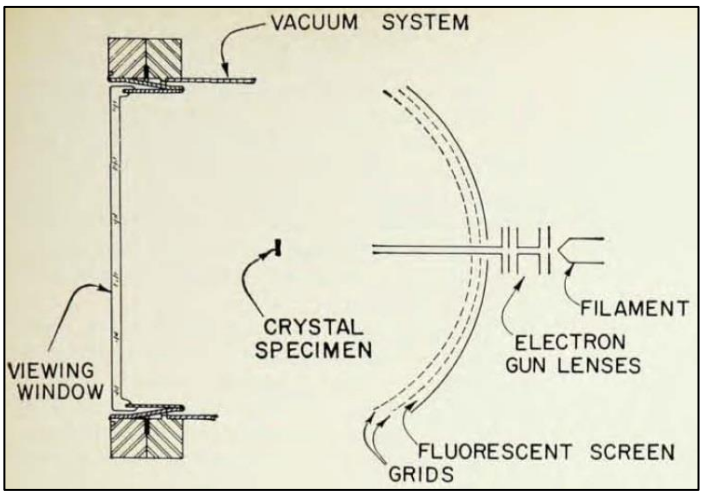

FIG. 3.9. Scheme of the working principle of the LEED technique [47].

In order to generate a diffraction pattern, the sample must be a single crystal with well-ordered surface structure. Only the elastic scattered electrons contribute to the pattern and the secondary electrons are removed by energy-filtering grids placed in front of the fluorescent screen.

When using LEED, it is common to determine the structure of a solid surface when the bulk structure of the material is already known by other means [48]. LEED can provide essentially two levels of information:

1) The analysis of the spot positions provide information on the symmetry of the surface structure (size and rotational alignment of the adsorbate unit cell with respect to the substrate unit cell).

2) Recording the intensity of diffracted beam as function of incident electron energy it is possible to determine the absolute dimensions of the surface unit cell. This requires however the comparison of the experimental data with an adequate theoretical model.

Sophisticated calculations, generally run on a workstation, can provide atomic coordinates with a typical precision of ±0.05 Å, which is generally more than adequate to determine the adsorption site of a molecule or the atomic positions in a reconstructed surface.

Chapter 4
Surface preparation and structural properties

In this chapter we present the experimental results concerning the structural properties of the studied (20-21) InGaN samples, i.e. the surface morphology by atomic force microscopy (AFM), the polarity determination by X-ray electron spectroscopy (XPS) and the investigation of the surface structure by low energy electron diffraction (LEED). Furthermore, we also discuss the steps and the measurements involved in the preparation of a clean InGaN surface: we compared the results obtained for thermal annealing in vacuum and nitrogen ambient.

4.1 Properties of the studied InGaN samples

The structural properties of the investigated samples are showed in figure 3.1. HVPE-grown bulk substrates with a semipolar (20-21) orientation were used, with threading dislocation density on the order of 10^6 cm^{-2}. The growth was performed using metal-organic vapor phase epitaxy (MOVPE).

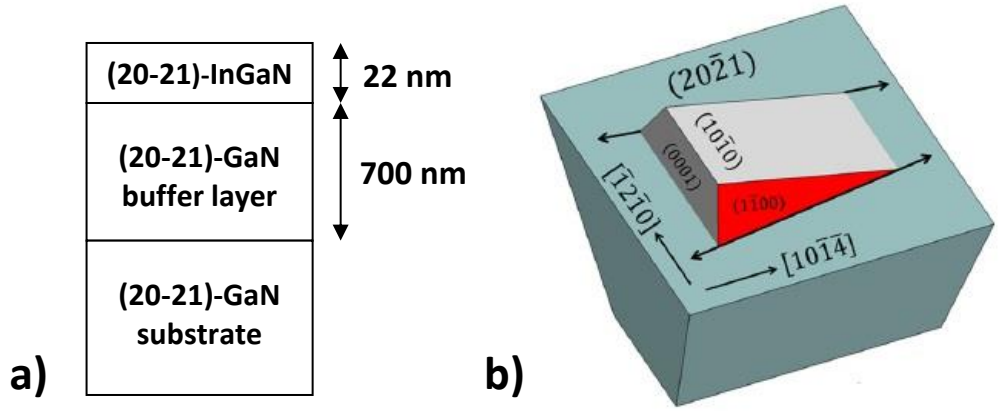

FIG. 4.1. Properties of the investigated samples: a) multi-layer structure and b) orientation of the wurtzite unit cell relative to the (20-21) orientation [32].

First, 700 nm of undoped GaN was grown using TMG and NH_3 as precursors, and H_2 as a carrier gas, at a temperature of 980 °C and pressure of 50 mbar. Subsequently the temperature was reduced and pressure increased to 400 mbar, and 22 nm of InGaN was grown using N_2 as a

carrier gas, and TEG, TMI and NH_3 as precursors. Growth temperatures for InGaN were nominally 725 C and 750 C resulting in two samples with an indium composition of 10.2% and 6.5%, respectively. These values, determined by x-ray diffraction (XRD), have two justifications:

1) In the range of low indium concentration the InGaN samples are expected to exhibit a relatively flat surface and a low density of defects. These properties are desirable to have a high quality material for the applications.
2) The small difference between the two values allows to investigate the effect of the indium content in this range and simultaneously to check the accuracy of certain surface experimental techniques.

The polarity of the InGaN layers is predicted to be group-III polar according the to the polarity of the GaN layer underneath.

4.2 Morphology of oxidized surface

Before cleaning the samples with the appropriate surface preparation methods, the morphology was investigated with atomic force microscopy (AFM). We used the AFM microscope in semicontact mode, which allows to acquire simultaneously two different kind of images, topography and phase contrast. Because the InGaN samples are grown on free-standing GaN substrates, a very low lattice mismatch is expected, and thus a very low density of misfit dislocations. However, the samples contain threading dislocations, which are probably due thermal and chemical fluctuations during the growth. The density of threading dislocations (TDs) in the GaN substrate is approximately around 10^6 cm^{-2} [49]. The density of V-pits on the surface of the InGaN top layer should be roughly of the same order of magnitude of the density of TDs in the GaN layer. This value does not allow the observation of V-pits with AFM or TEM, i.e. to observe one V-pit one would require at least an AFM image of (100 μm x 100 μm).

Figure 4.2 illustrates (2 μm x 2 μm) AFM images of the InGaN surface. The surface appears very smooth and exhibits undulations. The phase contrast image doesn't show significant features which not correspond to the topography, indicating a nearby homogeneous strain distribution. The very low roughness and the uniform strain distribution are both indicators of a high-quality samples. The observed undulations are parallel to each other and have an amplitude which varies roughly from 1 nm to 2 nm, as shown in figure 4.3.

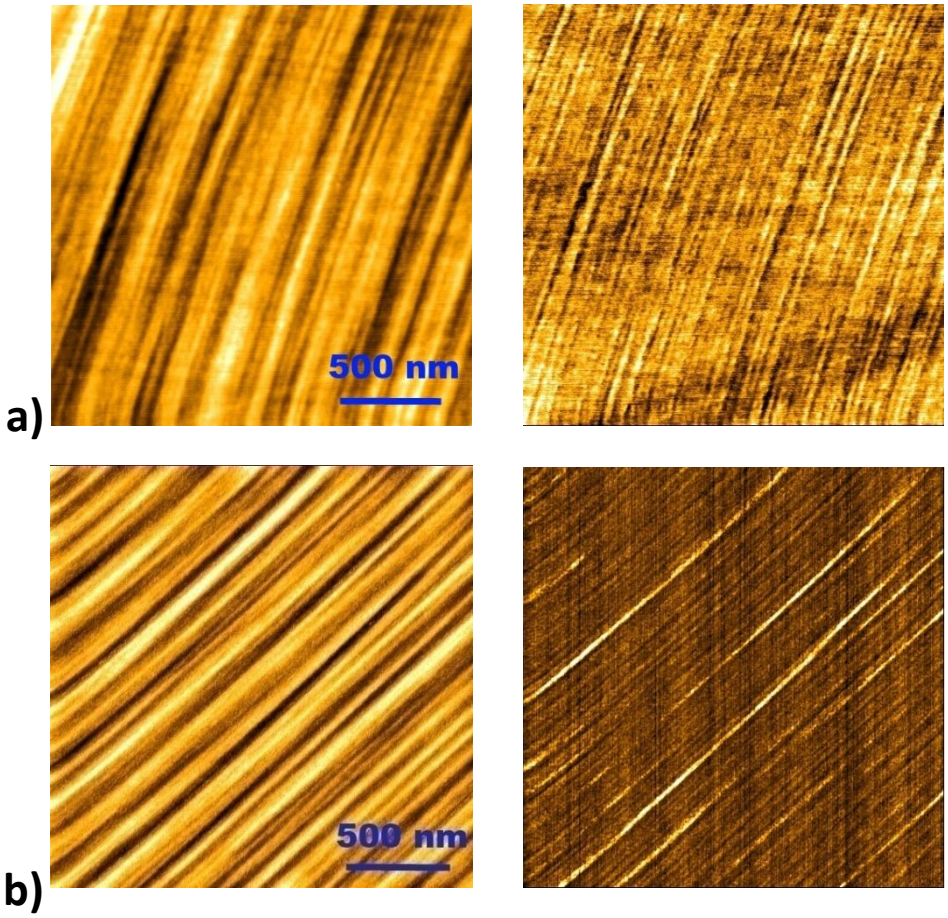

FIG. 4.2. 2x2 μm² AFM images of the InGaN oxidized surface: topography (left) and the corresponding phase contrast (right) of the sample with indium content a) 10.2 % and b) 6.5 %.

The estimation of the mean undulation period is done by counting the number of oscillations in a cross section profile of the topography. The results of a statistical analysis over around 10 different images are showed in table 4.1. The surface roughness and the mean undulation period are very similar for the two InGaN samples. From these measurements, it is not possible to distinguish between the two different indium contents. However, a source of uncertainly is the detection of sharp peaks in the profile which could be related to measurement artefacts. Actually, a clear separation is not always possible in the observed profiles due to the different shapes of undulations. Ploch et al. [23] reported about (20-21) InGaN layers with indium content below 3% and undulation period around 35 nm. Conversely, our measurements characterize morphology undulations with period around 180 nm. This difference seems not to be supported only by the difference in indium content. Further investigations are needed in order to understand the relation between indium content and morphological properties.

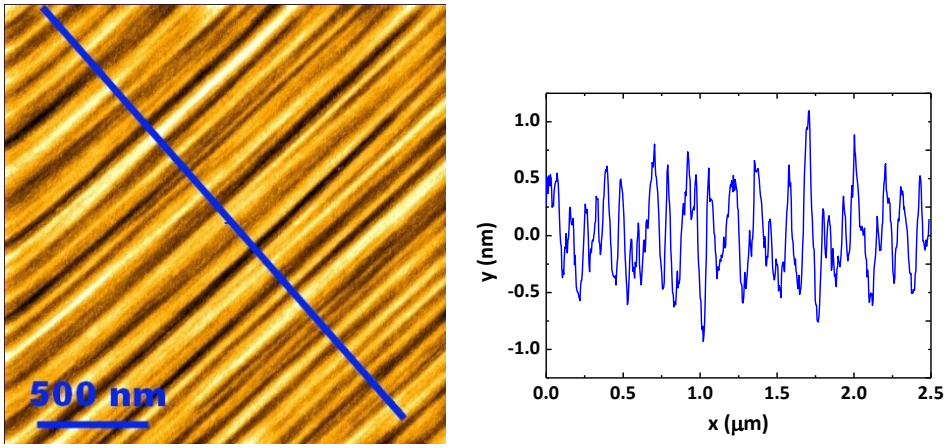

FIG. 4.3. 2x2 µm AFM topography image of the InGaN sample with 6.5% indium and a cross section profile which shows the undulations.

In %	surface roughness (nm)	undulation period (nm)
6.5	0.48 ± 0.07	170 ± 30
10.2	0.41 ± 0.04	190 ± 30

TABLE. 4.1. Surface roughness and mean undulation period and corresponding standard deviations over a range of 10 different AFM images.

The fact the morphology appears quite the same before and after the thermal annealing support the idea that the surface undulations are related to the underlying bulk structure. The presence of surface contaminants could be affect a particular surface reconstruction, but this is excluded by LEED measurements discussed in section 4.6.

4.3 Thermal annealing

The surface preparation method of thermal annealing has been used in two different variants: in UHV and in nitrogen ambient. In the first case, three different annealing temperatures were investigated. After annealing for 10 minutes at a certain annealing temperature, the sample was rotated to the Auger electron analyzer and the composition of the surface was investigated using Auger electron spectroscopy (AES). As shown by the spectra in figure 4.4a, an actual reduction of carbon compounds on surface is observed. Similar spectra are obtained for the InGaN sample with 6.5%

indium (not shown here). The missing reduction of oxygen contaminants is probably due to the very low amount of native oxygen on the surface, around 3%. The III-V ratio is initially low and further decreases with increasing annealing temperature (spectrum 4.4b). This reduction could be related to a small indium diffusion. However, the estimation of the III-V ratio is affected by an error due to the different escape depths of electrons of Gallium and Nitrogen. So, the measurements showed in figure 4.4b indicate rather a III-V ratio of (0.8 ± 0.1).

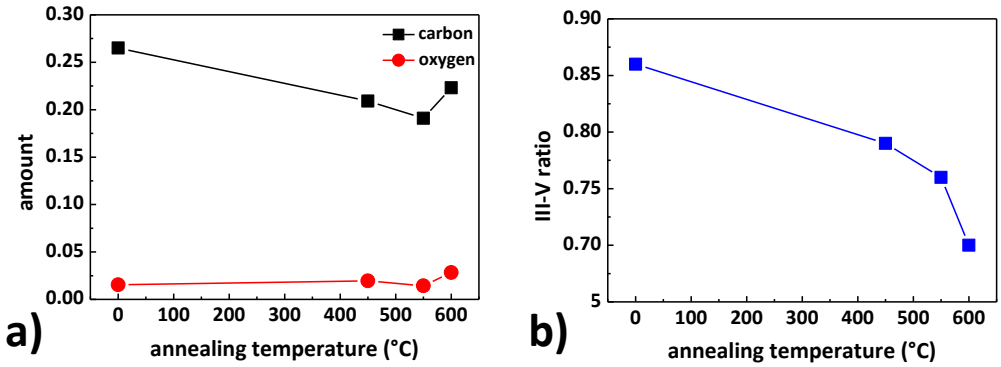

FIG. 4.4. AES spectra on the InGaN sample with 10.2% indium: a) amount of contaminants and b) III-V ratio as function of the annealing temperature.

After the first set of thermal annealing operations the samples are again exposed to air and transferred in another UHV chamber equipped with a N_2 plasma generator. One the one hand the thermal annealing in nitrogen ambient is supposed to be more efficient than thermal annealing in UHV, on the other hand this cleaning operation is more complicated to realize than the second. For this reason, in this case, the samples are subjected to just one annealing temperature of 550 °C for 15 minutes. After that, the sample are transferred in the chamber with the XPS spectrometer.

	6.5% indium		10.2% indium	
Ratio	oxidized	annealed	oxidized	annealed
C/Ga	0.32	0.08	0.33	0.14
O/Ga	0.12	0.03	0.15	0.01

TABLE 4.2. amount of contaminants relative to gallium before and after annealing in nitrogen ambient.

The XPS analysis with the two software *Casa XPS* and *Spec LAB* yields the results indicated in table 4.2. The results showed in table 4.2 indicate a significant reduction of oxygen and carbon contaminants on the surface. This is also confirmed by the spectra in figure 4.5 in which the XPS peak of the contaminant are compared before and after annealing.

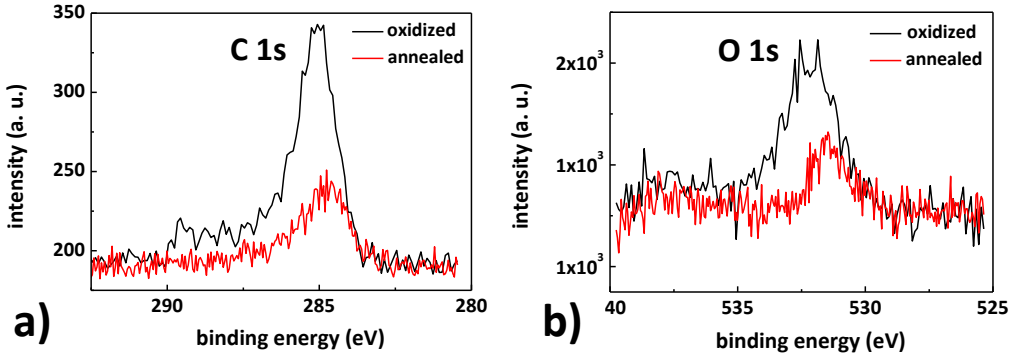

FIG 4.5. XPS peak of the a) C 1s and the b) O 1s level.

In comparison with thermal annealing in UHV, we conclude that thermal annealing in nitrogen ambient is a more efficient surface preparation method even at lower temperatures. This conclusion is in agreement with the results of J. Falta [38].

4.4 Stoichiometry

As mentioned in the previous section, the different escape depths of indium and gallium do not allow a correct estimation of the III-V ratio or In/Ga ratio with AES. However, in the case of the XPS technique the In/Ga ratio can be estimated more accurately (table 4.3).

	6.5% indium		10.2% indium	
In/Ga	oxidized	annealed	oxidized	annealed
bulk	0.08	0.09	0.13	0.13
surface	0.08	0.06	0.03	0.03

TABLE 4.3. In/Ga ratio in the surface of the two samples estimated by XPS.

Two important facts. First, the In/Ga ratio agrees approximately with XRD results. Although the average indium content in the heterostructure and the XPS measured In/Ga ratio are, strictly speaking, two different physical properties, it is reasonable that they do not differ significantly to each other. Second, the In/Ga remains the same after the annealing process indicating no structural changes induced by the cleaning procedure.

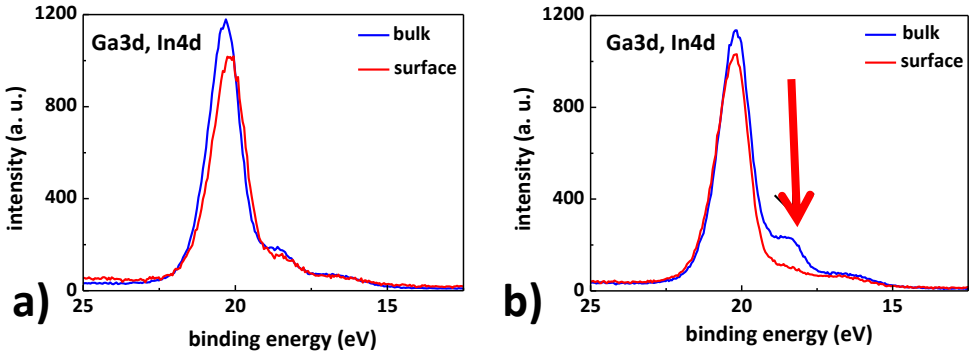

FIG 4.6. XPS Ga3d and In4d peaks of the InGaN sample with indium content of a) 6.5% and b) 10.2%. The arrow indicates a different indium component.

An unsolved issue is related to the differences in In/Ga ratio between the bulk-sensitive and surface-sensitive measurement conditions. These differences are evident even if we compare the Ga3d/In4d peaks of the two samples in figure 4.6, where the arrow indicates a different indium component. A way to explain these differences is to assume that the indium diffusion is more significant in the sample with greater indium content. However, the difference in indium content between the two samples is too small to explain such differences in the peaks. A more accurate analysis finalized to the separation of the core level peaks require a suitable fitting procedure of the XPS peaks.

4.5 Polarity determination by XPS

As reported by Skuridina et al. [10], the polarity of InN and GaN layers can be suitably determined by XPS, analyzing the intensities of the valence band electrons in the XPS spectrum. If the peak at higher binding energies dominates, then the sample is N-polar, vice versa, if the peak at lower binding energies dominates, then the sample is group-III-polar. Since the samples investigated here are InGaN layers with low indium content, we expect that the polarity determination method works also in our case.

The valence band spectrum was acquired for two different configurations of the samples (figure 4.7). In the first configuration, the electrons are emitted along the (20-21) direction. In the second configuration, the sample is tilted about 75 degrees with respect to the first configuration and the electrons are emitted along the c-direction.

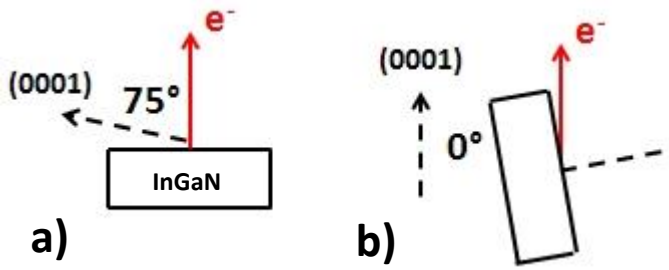

FIG 4.7. Configurations of the samples during the XPS valence band analysis. The electrons are emitted along a) (20-21) direction and b) c-direction.

Actually, the polarity determination method by XPS has been demonstrated appropriate also for the investigated InGaN samples. Since the polarity is a property of the c-direction, in the case of configuration a) of the sample, one doesn't expect a peak domination in the valence band spectrum. This is observed in the spectrum shown in figure 4.8.

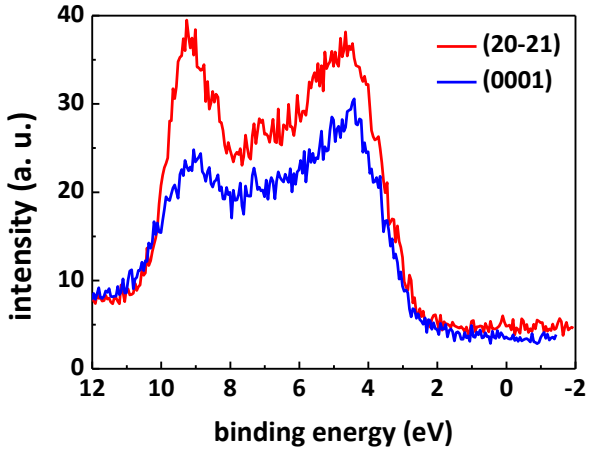

FIG 4.8. Valence band of the InGaN sample with 10.2% indium. The XPS spectrum was acquired for two different emission directions of the electrons.

The XPS valence band spectrum is instead dominated by one peak in the case of the configuration b) of the sample. The dominated peak corresponds to lower binding energies, so the polarity of the sample is deduced to be group-III-polar.

4.6 Surface reconstructions by LEED

After the surface preparation and characterization, the structural properties of the surface were investigated. The surface structure of the samples was investigated by the acquisition of LEED patterns with different energies. No differences between the LEED images of the samples with 6.5% or 10.2% indium content were observed. Also after exposing the samples to annealing temperatures of 450 °C or 600 °C the patterns don't change. Two significant LEED patterns taken at different energies are shown in figure 4.8.

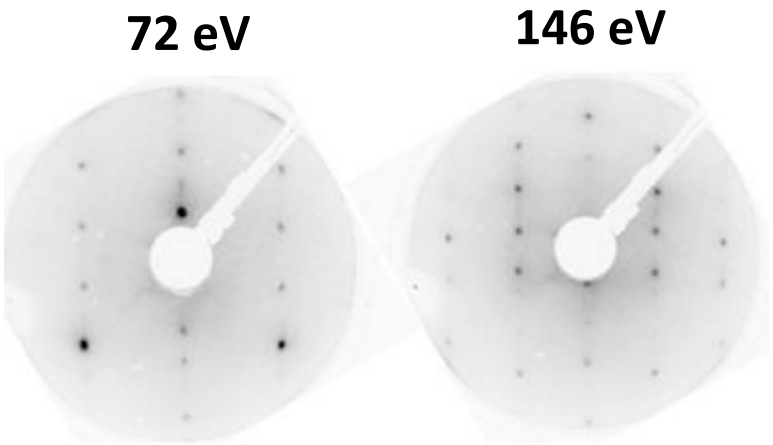

FIG. 4.8. LEED patterns of the clean (20-21) InGaN surface taken at two different energies.

The LEED images appear very bright with clear spots, and are indicative of the good quality of the samples and of the efficiency of the surface preparation. In figures 4.9 two different surface unit cells are superimposed on the LEED patterns. We suggest these structures taken into account the structural model for the (20-21) surface proposed by Yamashita et al. [22]. In figure 4.9a we propose a (2x4) surface reconstruction and in figure 4.9b we propose a c(2x8) surface reconstruction. However, beside of the good quality of the LEED experimental patterns, it remains still difficult to identify a unique surface unit cell. This difficulty is related to the interrelation between intensity of the spots and different factors, which can lead to vanishing spots in positions where it is not expected.

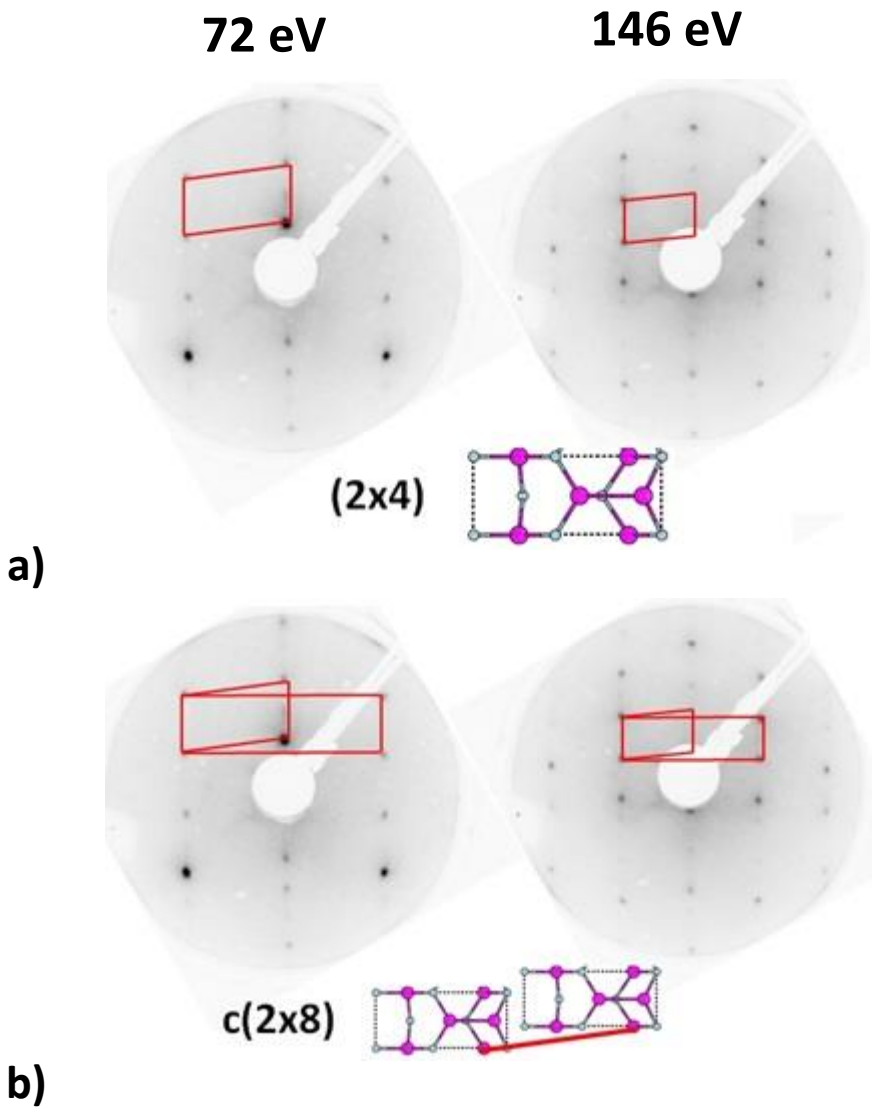

FIG. 4.9. LEED patterns of figure 4.8 with schematic representation of a possible surface unit cell; a) 2x4 surface unit cell, b) c(2x8) surface unit cell.

To identify the surface reconstruction showed in these experimental patterns, the comparison with a structural model of the (20-21)-InGaN surface is required. Nevertheless, a structural model of the (20-21) surface was proposed recently by Ploch [23]. We discuss the compatibility of this model with our experimental results in section 5.2.

Chapter 5
Electronic and optical properties

In this chapter we consider the results concerning the electronic and optical properties of the InGaN samples. Scanning tunneling microscopy (STM) allows to identify features at two different length scales, which are presumably related to the surface morphology. The band bending is investigated with X-ray photo-electron spectroscopy (XPS). The energy gap of both GaN and InGaN in the InGaN/GaN heterostructures is measured with surface photovoltage spectroscopy (SPS), and is also compared with the results obtained with Scanning tunneling spectroscopy (STS) and optical transmission.

5.1 Calibration of STM on HOPG films

The reproducible preparation of tunneling tips is one of the experimental key aspects of STM. Indeed, a suitable tunneling tip is the prerequisite for obtaining both high quality STM images and reproducible spectroscopic data. Two relevant attributes of a tunneling tip are shape and chemical composition. Contaminants can lead to distortion of the STM image. For example, insulating layers covering the tip apex such as metal oxides act as additional tunneling barriers which the electron have to overcome.

A widely used element for STM tips is tungsten. It has a high and smooth density of states at the Fermi energy, so that it is feasible for spectroscopic measurements. In addition, tungsten is mechanically stable and it can be used even at low temperatures. The most common method to produce sharp metallic tips is electrochemical etching. A piece of tungsten wire with diameter of around (0.2 ÷ 0.4) mm is mounted to a holder and immersed into NaOH solution. A ring-shaped stainless steel wire is situated concentrically around the W anode and serves as counter electrode. If a voltage is applied between the two electrodes, the following reaction takes place:

$$W(s) + 2H_2 = +2OH^- \rightarrow WO_4^{2-} + 3H_2(g)$$

The dissolution of tungsten causes the formation of a neck on the wire. As the reaction proceeds, the neck becomes thinner and thinner until if finally

breaks and the lower part drops off. The resulting tip has a radius of apex curvature in the order of about 20 nm to 50 nm [44].

After mounting a new metallic tip in the STM microscope it is important to perform a calibration in order to check the reliability of the succeeding measurements. The calibration of the STM apparatus includes both the acquisition of an atomic-resolved STM image and the acquisition of a IV curve in the spectroscopic mode. A well-studied material, suitable for the calibration of STM, is HOPG (Highly Ordered Pyrolytic Graphite).

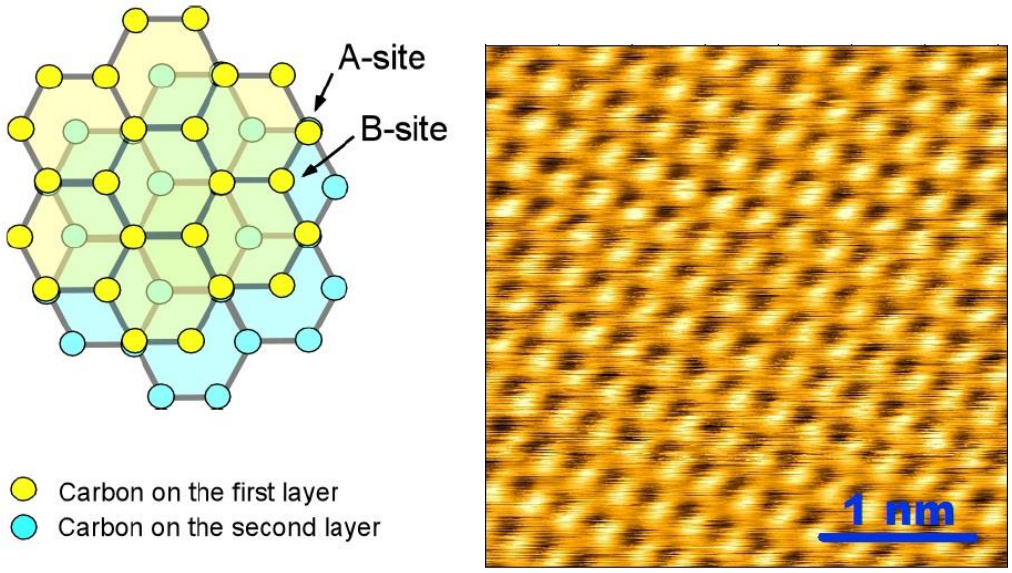

FIG. 5.1. a) layered structure of HOPG [50] and b) acquired STM image of a HOPG film.

The STM image of a HOPG sample shows a honeycomb structure, known as "three-fold-hexagon" pattern (figure 5.1a). HOPG consists of carbon sheets, forming a semi-metallic system. While the carbons within a sheet are covalently bonded to form a hexagonal lattice structure, the layers are held together by the Van der Waals forces. The sheets are arranged such that the every other carbon on a layers has a carbon in the neighboring sheets, as shown in figure 5.1a. The carbons in the first layer that have a carbon in the second layers right below are called A-site carbons, and the carbons without a carbon directly below are called B-site carbons [50].

Under ideal conditions, STM images of HOPG surface reveal a lattice of dark spots with a lattice parameter of 0.246 nm. From our STM images images we found a lattice constant of (0.257 ± 0.006) nm, which is in quite good agreement with the reported value. The small deviation could be related to thermal drift effects which produce a distortion of the STM

images. The measured IV curve of the HOPG film is showed in the section relative to the STS measurements (figure 5.13, section 5.5).

5.2 STM images of the InGaN samples

After performing the calibration of the STM tungsten tip, STM images of the InGaN samples are acquired in UHV conditions. The STM images exhibit undulations at two different length scales. In images bigger than (200 nm x 200 nm) the undulations are clearly seen, as in the case of the AFM images (section 4.1). Furthermore, in the atomically resolved range, i.e. in images smaller than 20 x 20 nm, kind of nano-undulations are observed locally.
Figure 5.2 shows a STM image and a corresponding cross-section profile of the undulated features. These features are supposed to be related to the morphology undulations observed in the AFM images (section 4.1).

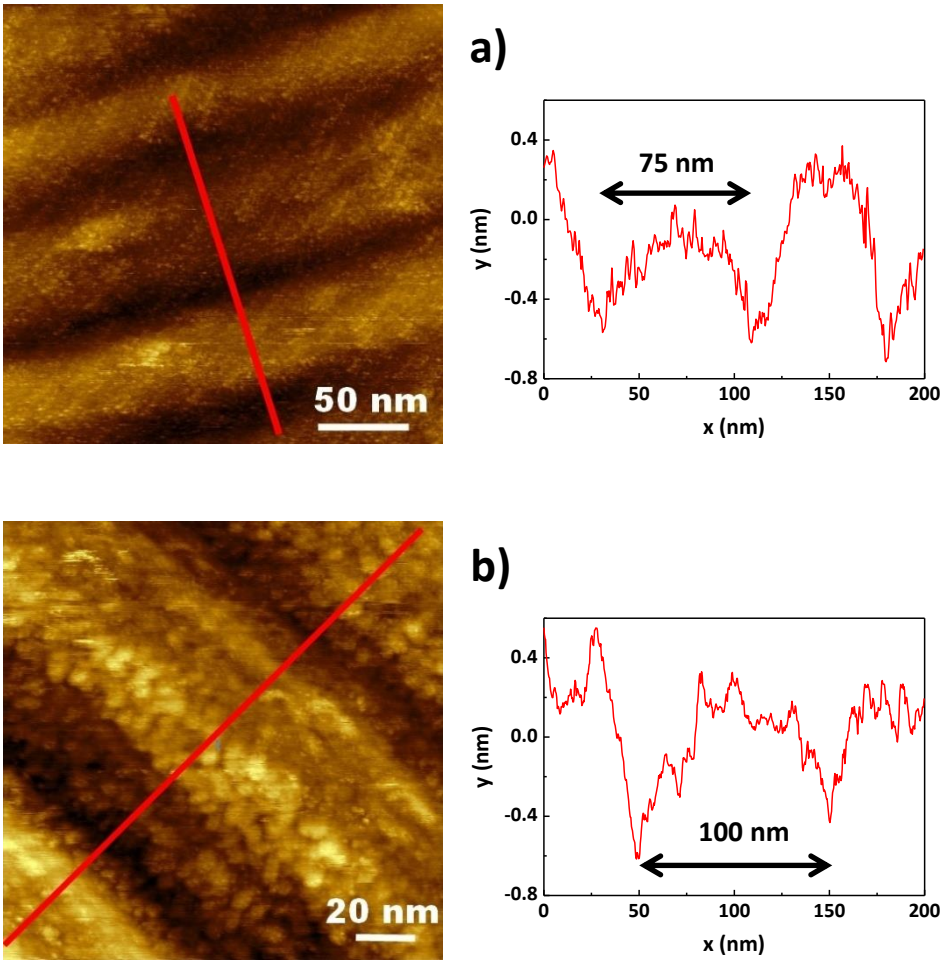

FIG. 5.2. STM images and corresponding cross section profiles of the InGaN sample with indium content of a) 6.5% and b) 10.2%.

In fact, in the case of STM images the undulations belong to the electronic density of states (DOS). One can infer that the DOS follows roughly the atomic structure at the surface, but no exact correspondence is expected. Howsoever, the identification of undulations with both experimental techniques is an interesting aspect. As reported in section 4.1, the undulation period in the morphology is around (170 ÷ 200) nm. From the cross-section profiles of the electronic density in figure 5.2, we deduce instead an undulation period of (70 ÷ 100) nm. As explained in section 2.2, the undulated morphology is apparently related to the semipolar orientation of the investigated samples. In addition, because a similar pattern is observed with both AFM and STM techniques, we conclude that the undulations are real and not related to artefacts. However, because different physical effects are involved during the tip-surface interaction for the two scanning probe techniques, it is not clear if it is possible to define a quantitative relation between the two kind of undulations. Beside of the high quality of the acquired images, the estimation of the mean undulation period remains still difficult and leads to a relatively high uncertainty.

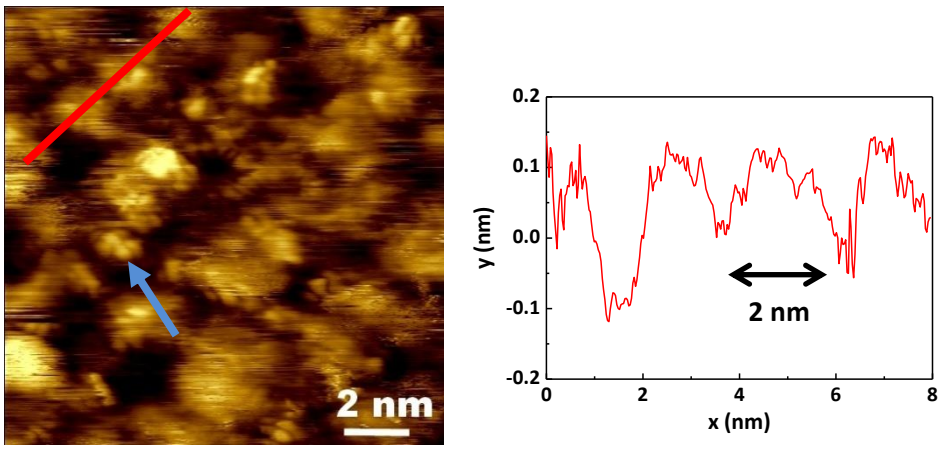

FIG. 5.3. STM image and corresponding cross-section profile of the InGaN sample with 6.5% indium. The image shows the possible presence of nano-undulations of period around 2 nm. The blue arrow indicates a group of 4 atoms.

Figure 5.3 indicates a STM image with nano-undulations and their corresponding cross-section profile. The nano-undulation period is 2 nm. If we consider the model of the (20-21)-GaN surface proposed by Ploch et al. [23], we note that our measurement could represent an effective observation of this structural undulation. Assuming that the observed nano-undulations are not related to the presence of a unusual surface reconstruction, we expect that the morphology of the clean (20-21) surface

of our InGaN samples in normal conditions is quite similar to the morphology of the (20-21) GaN samples. As shown in figure 5.4, a undulation period of 2 nm is compatible with the structural model of the (20-21) surface. Unfortunately, tip-related problems have not allowed to obtain a variety of clear STM images of the samples at the nanoscale. Hence, we cannot support our thesis with an appropriate statistics. However, the correspondence between the observed nano-undulation period of 2 nm and structural model seems to be very reasonable.

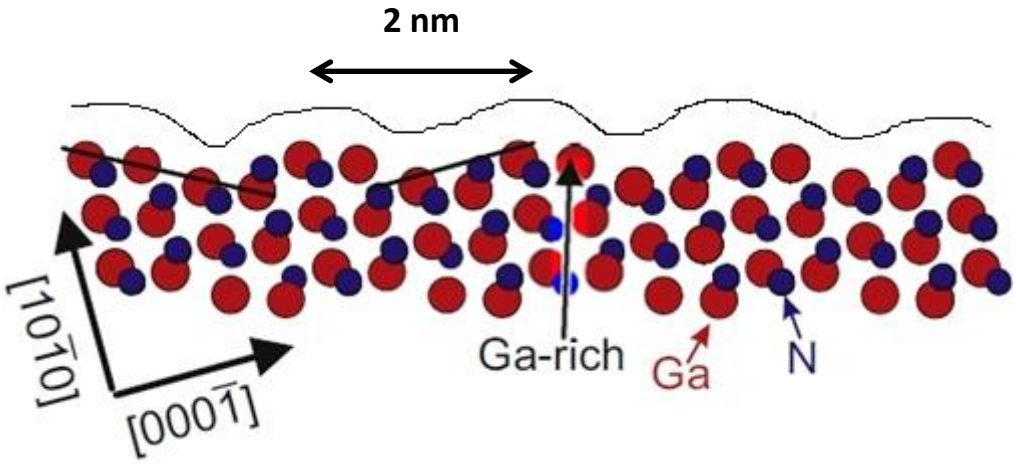

FIG. 5.4. Model of the (20-21) GaN surface proposed by Ploch et al. [23] already showed in chapter 2. In this image we indicate a undulated line profile over the top of the surface. The observed nano-undulation period of 2 nm is compatible with the model.

Figure 5.3 shows also groups of atoms (one of which is indicated by the blue arrow). Although the STM image is atomic-resolved, the presence of artefacts does not allow to deduce a clear atomic pattern in order to associate the visible atoms to a surface reconstruction.

5.3 Band Bending

Usually, an oxide layer is found on the surface of III-nitride semiconductors. The oxide layer act as a barrier and interfere with phenomena like tunneling and thermoionic emission which are important for applications. Few nanometers of oxide are sufficient to increase a Schottky barrier by significant fractions of eV [34]. Thus, it is desirable to reduce so much as possible the oxide layer on the semiconductor surfaces.

In our experiments, the barrier height is measured comparing the XPS spectra before and after the surface preparation by thermal annealing. One expects a shift of the XPS spectra because of the different

composition-induced electronic properties of the surface after the surface preparation. In order to know if this shift is localized to the valence band or if it concerns a wide part of the spectrum, one can compare the valence band and the indium core level peaks, which are characterized by a binding energy which is two order of magnitude higher. This comparison is showed in figure 5.5.

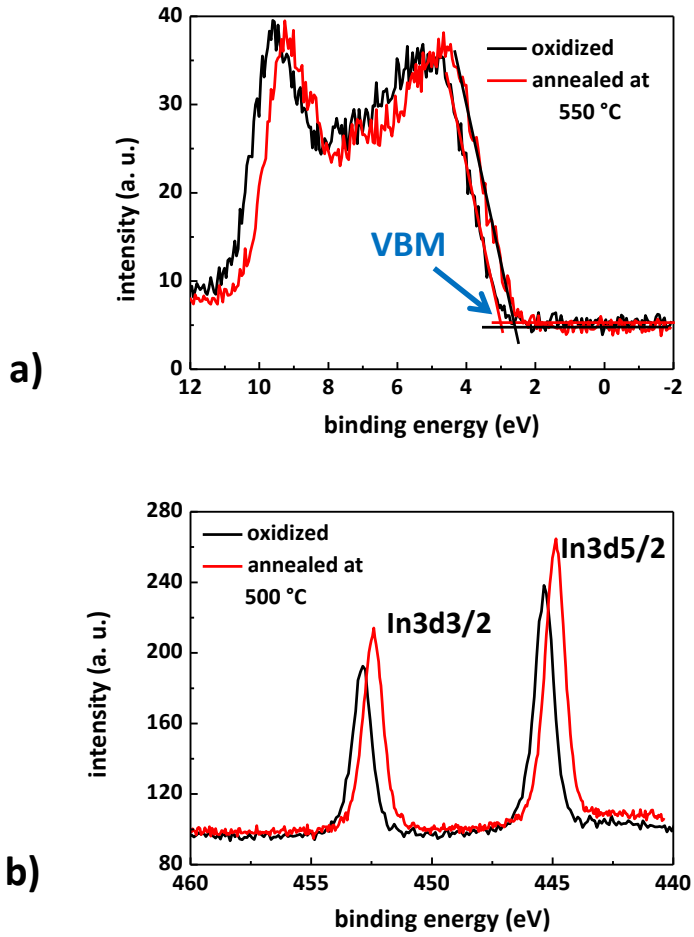

FIG. 5.5. XPS spectra of the InGaN sample with 10.2 % indium; a) valence band, b) indium core level peaks. The value of the valence band maximum (VBM) is extracted from figure a).

The valence band maximum (VBM) can be extracted from the valence band spectrum (figure 5.5a): it is represented by the intersection between the linear interpolation of the ground, around 0 eV, and that of the first slope change for increasing binding energy. As shown in table 5.1, the valence band and the indium core level peaks are both shifted and the energetic shift increases with the indium content. A shift of the valence band of InGaN alloys with different indium content is also reported by Veal et al. [20].

Valence band maximum (VBM)		
In %	oxidized	annealed
6.5	2.91 eV	2.81 eV
10.2	3.01 eV	2.58 eV

Energetic shift		
In %	VBM	In peaks
6.5	0.1 eV	0.3 eV
10.2	0.3 eV	0.5 eV

TABLE. 5.1. Values of VBM and of energetic shift extracted from the spectra showed in figure 5.5a and 5.5b, respectively.

Knowing the valence band maximum (VBM) and the energy gap E_g, both measurable quantities, one can estimate the barrier height Φ as

$$\Phi = E_g - VBM$$

As reported by Veal et al. for polar (0001) InGaN layers [20], we confirm that electron depletion occurs similarly on semipolar (20-21) InGaN layers.

Barrier height = E_g – VBM		
In %	oxidized	annealed
6.5	0.3 eV	0.4 eV
10.2	0.1 eV	0.5 eV

TABLE. 5.2. Values of VBM and of energetic shift extracted from the spectra.

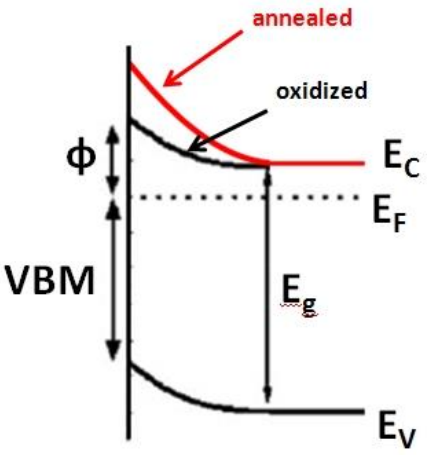

FIG. 5.6. Barrier height in a schematic band diagram.

In addition, we observe that the thermal annealing process leads to larger upward band bending. This is probably due to the oxidation-induced passivation of the surface. A larger barrier height is not desirable, so, the control of the indium content in the InGaN layers becomes essential to control as well as the surface band bending.

5.4 SPS measurements

The surface photovoltage spectroscopy (SPS) measurements were performed with two different experimental configurations. In the first configuration, the incident light interacts with the InGaN top layer. In the second one, the sample was tilted about 180 degrees, so that the incident light interacts with the free-standing GaN substrate, as shown in figure 5.7.

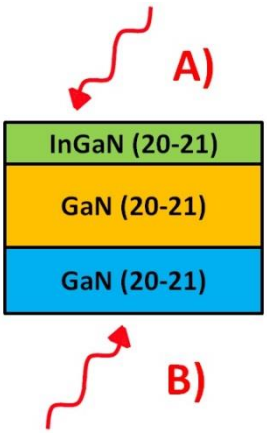

FIG. 5.7. Scheme of the two experimental configurations in the SPS experiments:

- **B) is GaN-sensitive**
- **A) is sensitive to both the InGaN layer and the InGaN/GaN interface.**

Because of the low thickness of the top InGaN layer, 22 nm, SPS measurements in configuration A) allow to investigate the InGaN/GaN interface. Thus, measurements in configuration B) are useful to have a reference spectrum of GaN and to identify more clearly the difference between the electronic properties of GaN and InGaN. The spectral resolution of the optical system is given by

$$\Delta\lambda = f\,\Delta l$$

where Δl is the slit width and f is a factor given by the instrument. In our case, f = 1.96 nm/mm and Δl = 3 mm, so that $\Delta\lambda$ = 5.88 nm. Now, the indetermination on the energy can be calculated from the relation between energy and wavelength

$$\delta E = hc\lambda^{-2}\delta\lambda$$

The SPS measurements are performed with a Xe lamp. The spectrum of GaN (configuration B) shown in figure 5.8b is obtained by normalizing the SPV spectrum of GaN relative to the SPV spectrum of the Xe lamp, both showed in figure 5.8a. The intensity of the incident light decreases rapidly in the range of the energy gap: because of this, the spectrum of GaN (figure 5.8b) is an increasing function and the energy gap is visible as slope

change and not as maximum. Anyway, the energy gap of GaN is an important feature in both spectra and is found to be equal to (3.47 ± 0.06) eV. The first slope change in the GaN spectrum, markes as E_V + 3.34 eV, is discussed later in connection with the InGaN spectra.

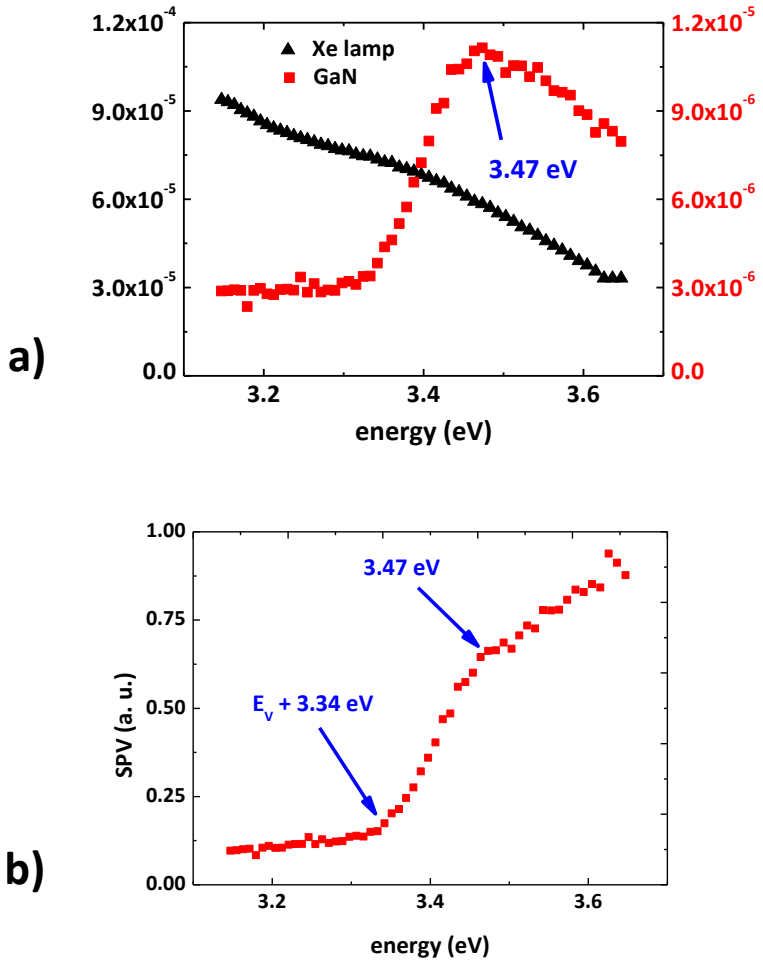

FIG. 5.8. SPV spectra in configuration B of a) GaN + Xe lamp, b) normalized GaN (with the indication of the two slope changes).

The SPV spectra relative to the InGaN (configuration A) are showed in figures 5.9 and 5.10. The SPV spectrum of the two InGaN samples is acquired for two different chopper frequencies: in this way, as the chopping frequency has a direct correlation with low-fast surface states, one can compare two different surface-sensitive levels. Beside of the spectrum intensity difference due to the different indium contents, which is higher for lower chopper frequency, the main features of the spectra are visible as slope changes of the curve in both cases.

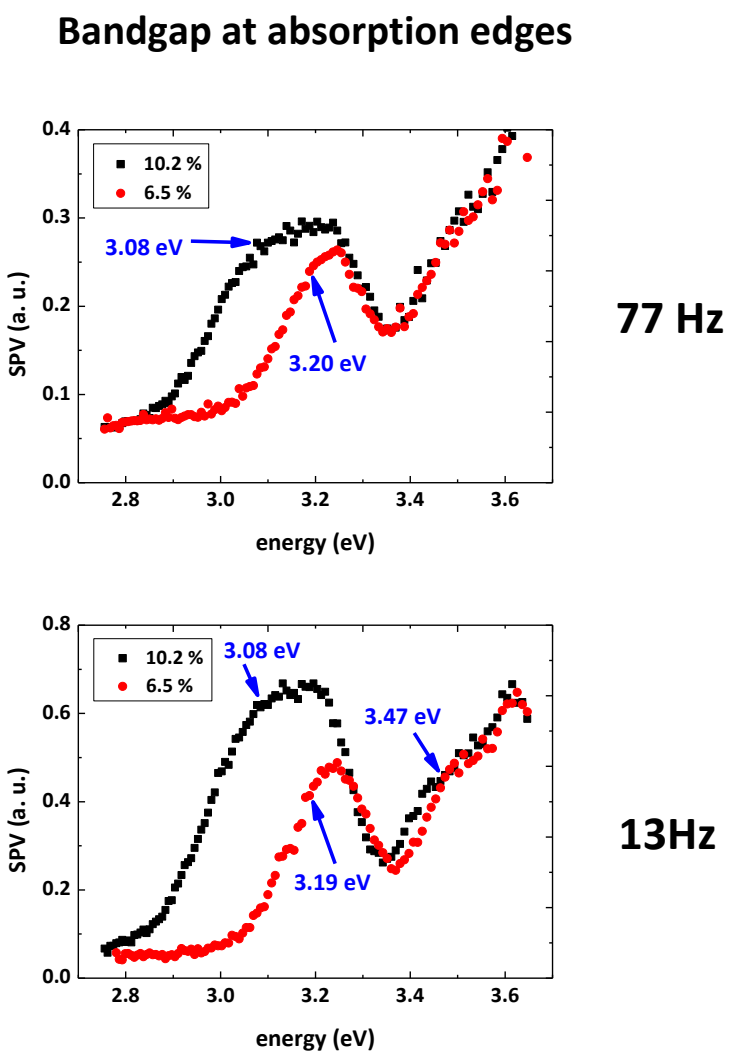

FIG. 5.9. SPV spectra of the InGaN samples (configuration a) acquired with two different chopper frequencies. Blue arrows indicate the slope change corresponding to the bandgap absorption edges of InGaN and GaN.

From these spectra (figure 5.9) it is possible to extract the values of the bandgaps of InGaN, which correspond to the energy values at which a negative slope change occurs. The results of the energy gap measurements are summarized in table 5.3. However, there are additional slope changes which correspond to other type of transitions, which are shown in figure 5.10. According to the notation of Kronik and Shapira [45], positive slope changes in the SPV spectra correspond to electronic transitions from the valence band, marked for example as E_V + X eV, while negative slope changes correspond to transitions to the conduction band, marked for example as E_C – Y eV. An interpretation of the InGaN SPV spectra showed in figures 5.9 and 5.10 is clarified in figure 5.12. Now we examine the physical meaning of the observed transitions.

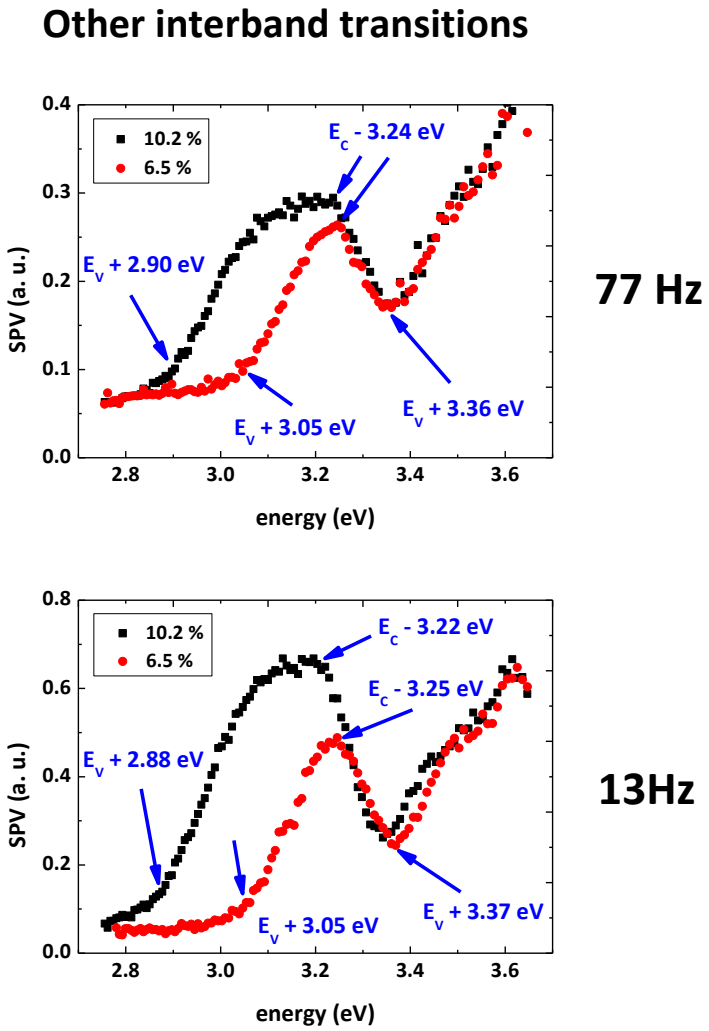

FIG. 5.10. SPV spectra of the InGaN samples (configuration A) acquired with two different chopper frequencies. Blue arrows indicate the slope change corresponding to different interband transitions, which are probably related to phenomena occurring at the InGaN/GaN interface.

The transitions below the bandgap of the InGaN samples, which depend on the indium content, could be related to defect states, whereas the transitions above the bandgap are probably related to electron-hole recombination at the InGaN/GaN interface. The transition E_V + 3.37 eV is independent from the indium content and is visible in both the GaN and InGaN SPV spectra. This suggests that the transition corresponds to the beginning of the GaN substrate. In fact, the transition takes place between the bandgap absorption edges of InGaN and GaN. The interpretation of the InGaN SPV is clarified in figure 5.12. In each spectrum, one can identify five different slope changes, which correspond to the following physical processes:

1) Transition from valence band to a defect state
2) Bandgap absorption edge of InGaN
3) Electron-hole recombination at InGaN/GaN
4) Beginning of the GaN substrate
5) Bandgap absorption edge of GaN

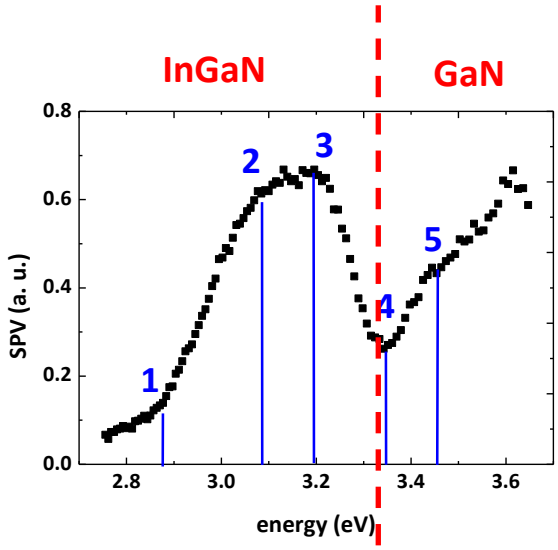

FIG. 5.12. Interpretation of the acquired SPV spectra showed in figures 5.9 and 5.10: there are five different slope changes corresponding to particular physical processes.

In heterostructures, there are further different possible electronic transitions due to the interfaces and interface-related defects.

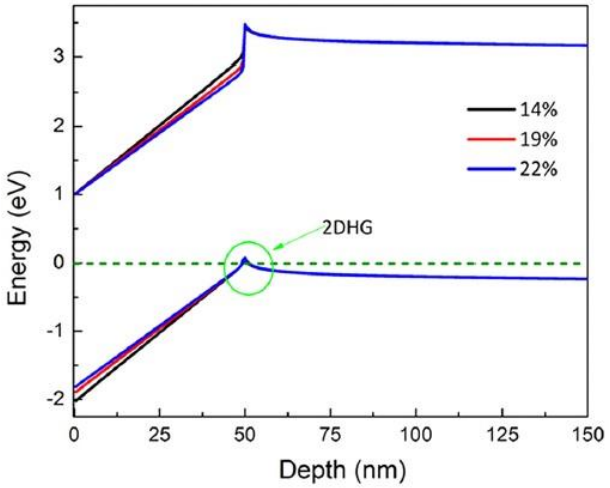

FIG. 5.13. Schrödinger-Poisson simulation shows conduction and valence band profile of undoped InGaN/GaN structures. The 2-dimensional hole gas (2DHG) accounts for the hole accumulation at the InGaN/GaN interface [17].

In order to identify more clearly the different electronic transitions one should consider a simulation of the band diagram of our materials. Pandey et al. [17] reported a Schrödinger-Poisson simulation for the band diagram of c-polar InGaN/GaN heterostructures with indium composition ranging from 14% to 22% (figure 5.13). In the band diagram, the existence of hole accumulation (2DHG) at the interface can be observed. If we assume that this diagram is qualitatively valid also for our semipolar InGaN samples, we infer that the transition E_V + 2.90 eV observed in the SPV spectra (figure 5.10) could be interpreted as a transition from the 2DHG to the conduction band. As shown in figure 5.13, a difference in indium content of 5% does not alter significantly the diagram (in our case the indium content is 10.2% and 6.5%).

In %	Energy gap (eV)
0	(3.46 ± 0.06) eV
6.5	(3.19 ± 0.05) eV
10.2	(3.08 ± 0.04) eV

TABLE. 5.3. Results of the energy gap measurements with surface photovoltage spectroscopy.

The results of the energy gap measurements are summarized in table 5.3. As shown in figure 5.11, our results are in quite good agreement with the experimental results of Pandey et al. [17]. The trend with a bowing parameter of b = 0.5 is found to be the best interpolation in the regime of low indium content.

$$E_g(x) = 3.40(1-x) + 0.67x - bx(1-x)$$

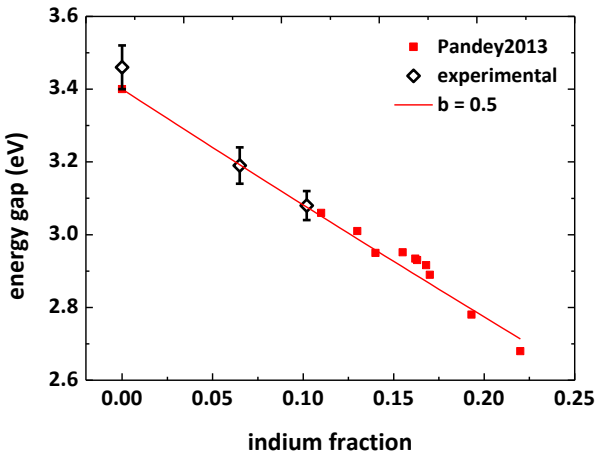

FIG 5.11. Plot of the energy gap results listed in table 5.3 and comparison with the results of Pandey et al. [17]. The line shows the calculated trend for a bowing parameter equal to 0.5.

5.5 STS measurements

The Scanning Tunneling Microscopy (STM) experimental apparatus allows also measurements of current-voltage (IV) curves on specific regions of the investigated sample. In the context of the STM technique, the measurement of IV curves is referred to as scanning tunneling spectroscopy (STS). The calibration of the STM apparatus include both the acquisition of an atomic-resolved STM image (figure 5.1) and the acquisition of a IV curve of the HOPG sample (figure 5.13). Since HOPG is conductive, the corresponding IV curve is expected to be linear in a certain regime of bias voltage around the origin.

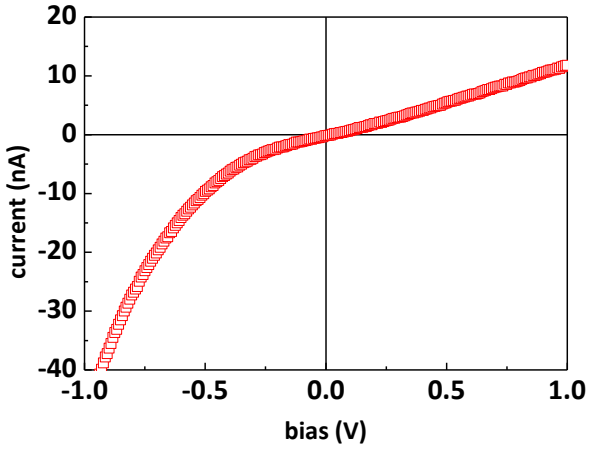

FIG. 5.13. measured IV-curve of the HOPG film which shows clearly a linear regime.

For the InGaN samples, the IV-curves are acquired in form of a square grid of 12 x 12 points in different areas of the sample. Figure 5.12a shows the mean IV-curve of a grid of around 20 x 20 nm acquired on the two InGaN samples with different indium content. Figure 5.12b exhibit the normalized differential conductivity from which the value of the energy gap is extracted, in agreement with the method described by Ebert et al. [51]. In table 5.4 we compare the measurements of the energy gap of the two InGaN samples performed by surface photovoltage spectroscopy and scanning tunneling spectroscopy. From these measurements, it emerges that a bandgap can be clear identified. However, the values of the measured bandgaps are much lower than the expected values. Further measurements are required to find out the origin of this significant difference.

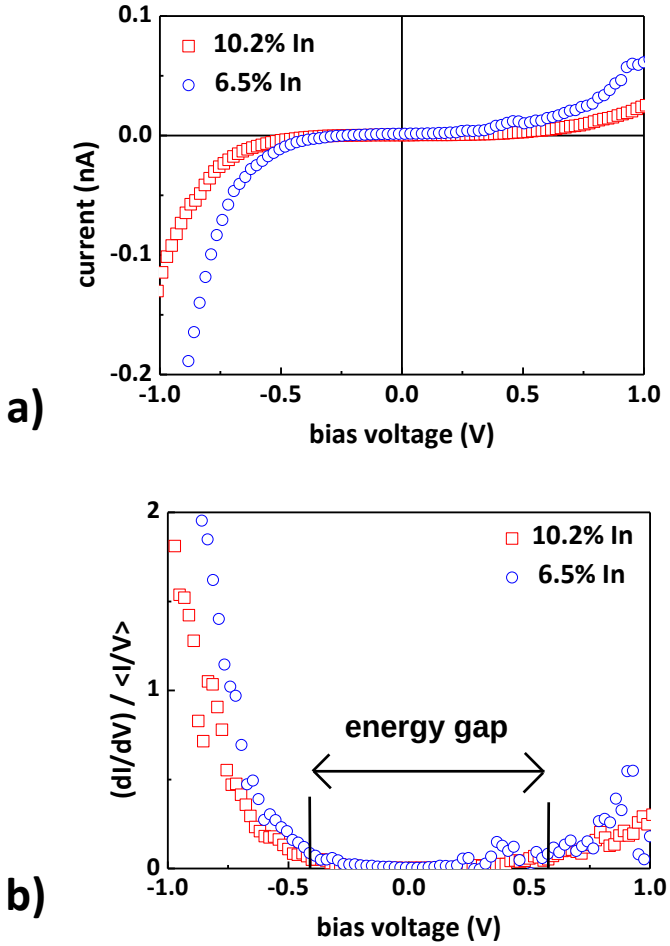

FIG. 5.12. a) IV-curve and b) normalized differential conductivity of the two InGaN samples.

In the case of STS, the values of the energy gap could be affected by the crystal structure or by tip-induced effects. The different information depth of the two techniques is also an important factor.

In %	Energy gap (eV) measured by SPS	Energy gap (eV) measured by STS
6.5	(3.19 ± 0.05) eV	(1.1 ± 0.2) eV
10.2	(3.08 ± 0.04) eV	(0.78 ± 0.07) eV

TABLE. 5.4. energy gap of the two InGaN samples measured with surface photovoltage spectroscopy and with scanning tunneling spectroscopy.

5.6 Optical transmission studies

In addition to SPS and STS measurements, we try to estimate the energy gap of the InGaN samples with optical transmission. SPS and optical transmission are in some way similar techniques. An important difference between the two techniques is that the SPS is surface-sensitive, whereas the optical transmission method is bulk-sensitive. Due to the structure of the investigated InGaN samples (figure 4.1), we expect that only the features of GaN are observable with the optical transmission method. The thickness of the two GaN layers together, the GaN substrate and the GaN buffer layer, is in the micrometer range, so, it is 2 order of magnitude greater than the thickness of the top InGaN layer, which is 22 nm. In fact, we try to measure the energy gap of GaN (not the gap of InGaN).

The optical transmission method is briefly described here. Once one has measured the optical transmittance, the absorption coefficient is obtained by the following procedure: in the region below the energy gap, where the absorption coefficient vanishes, the transmission coefficient is of the form

$$T = \frac{I_T}{I_0} = \frac{(1-R)^2 e^{-\alpha d}}{1-R^2 e^{-2\alpha d}} = \frac{1-R}{1+R}$$

Thus, assuming that the coefficient R does not depend on the wavelength λ, the expression for the absorption coefficient is

$$\alpha(\lambda) = -\frac{1}{d}\ln\left[\frac{\sqrt{(1-R)^4 + 4R^2T(\lambda)} - (1-R)^2}{2R^2T(\lambda)}\right]$$

Knowing that

$$\alpha \propto \sqrt{h\upsilon - E_{gap}}$$

one can extract the value of the energy gap E_g performing a best fit of the linear regime in the plot of α^2 as function of λ. The measured transmittance and absorption coefficient are showed in figure 5.13a and 5.13b, respectively. The interpolation of the absorption coefficient near the absorption edge, showed in figure 5.11b, allows an estimation of the energy gap of (3.2 ± 0.2) eV. This value is equal for both InGaN samples with indium content of 6.5% and 10.2%, as expected. The error on the energy gap, calculated form the errors on the linear fit, appears quite high.

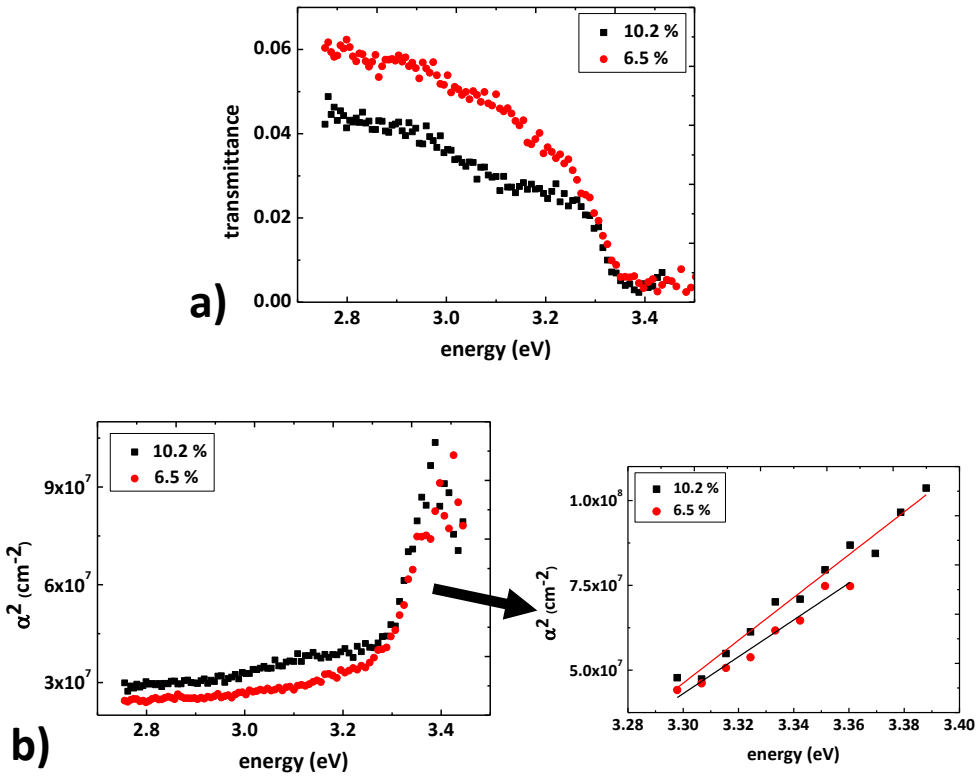

FIG. 5.13. a) transmittance and b) square of the absorption coefficient with the linear fit near the absorption edge.

Furthermore, this result is not in strict agreement with the energy gap of GaN measured with surface photovoltage, which is (3.47 ± 0.06) eV. We conclude that the energy gap measurement with surface photovoltage spectroscopy, beside of the different surface-sensitive level, is more accurate in comparison to measurement of the gap with optical transmission.

Summary and conclusions

The aim of this thesis was the investigations of the physical properties of the surface of semipolar (20-21) InGaN/GaN heterostructures. This was realized with a setup of surface-analytic experimental techniques, which yielded information on different aspects of the surface of the investigated samples. Most of these techniques required ultra-high vacuum conditions and appropriate surface preparation methods.

XPS and AES measurements allows the estimation of the elemental composition of the surface. The application of those techniques before and after the surface preparation allowed to demonstrate a significant reduction of surface contaminants (up to 70% for carbon and 80% for oxygen). This yields the conclusion that thermal annealing in nitrogen ambient is a very efficient method to obtain clean surfaces.
With XPS, the intensity of the band bending was evaluated, founding a barrier height of (0.1 ÷ 0.3) eV before thermal annealing and of (0.4 ÷ 0.5) eV after thermal annealing. We notice that surface electron depletion occurs similarly on semipolar (20-21) InGaN layers, as observed on polar (0001) InGaN layers by Veal et al.
The surface morphology of the InGaN layers, investigated using AFM, is characterized by undulations of amplitude between 1 nm and 2 nm, and period between 150 nm and 200 nm. Undulations exhibiting a period between 70 nm and 100 nm were observed also on STM images. These features are supposed to be related to the semipolar orientation of the InGaN samples. Moreover, the undulations in STM images at atomic scales show a periodicity of 2 nm, which is in quite exact agreement with the structural model of the (20-21) surface recently proposed by Ploch et al. A surface reconstruction on the InGaN samples was identified using LEED. It was not possible to determinate a unique surface unit cell, so, two different models are proposed.
The energy gap of both GaN and InGaN in the InGaN/GaN heterostructures was measured with SPS and was also compared with the results obtained with STS and optical transmission. The results obtained with SPS (i.e. the SPV method) are in good agreement with recent measurements performed by Pandey et al., although the choice of the value of the bowing parameter still remains a controversial. The SPV method has been confirmed a suitable method for the measurement of the energy gap and the observation of interband transitions in a multi-layer structure. However, a suitable simulation of the band diagram of the (20-21)

InGaN/GaN heterostructure is required for the interpretation of the observed interband transitions.

In conclusion, it was observed that certain physical properties as the energy gap and the barrier height for the surface electron depletion have comparable values in the case of polar (0001) and semipolar (20-21) InGaN layers. The observed surface morphology, instead, is related specifically to the semipolar growth orientation of the samples. Our STM and LEED results are oriented to the development of a structural model of the semipolar (20-21) surface. Further atomic-resolved STM images would be helpful to give a more clear picture of the semipolar (20-21) InGaN surface.

References

[1] R. M. Farrell et al., *Materials and growth issues for high-performance nonpolar and semipolar light-emitting devices*, Semicond. Sci. Technol. 27 (2012)

[2] Editorial, *Non-polar and semipolar nitride semiconductors*, Semicond. Sci. Technol. 27 (2012) 020301

[3] M. Grundmann, *The physics of semiconductors*, Springer-Verlag Berlin Heidelberg 2006

[4] M. Gonschorek, *Physical properties of AlIN/(AlN)/GaN ($0.07<x<0.23$) heterostructures and their application for high power electronics*, phd thesis 2010

[5] Duc V. Dinh, *MOVPE growth of InN and InGaN with different surface orientations*, phd thesis 2012

[6] S. Ploch, *Metallorganische Gasphasenepitaxie von semipolaren III-Nitrid Heterostrukturen und Lichtemittern*, phd thesis 2013

[7] T. D. Veal et al., *In adlayers on c-plane InN surfaces: A polarity-dependent study by X-ray photoemission spectroscopy,* Phys. Rev. B 76, 075313 (2007)

[8] P. Ruterana et al., *The microstructure and properties of InN layers,* Phys. Stat. Sol. C 7, 1301 (2010)

[9] D. Muto et al., *Polarity determination of InN by wet etching,* Phys. Stat. Sol. A 202, 773 (2005)

[10] D. Skuridina, *Polarity determination of polar and semipolar (11-22) InN and GaN layers by valence band photoemission spectroscopy*, J. Appl. Phys. 114, 173503 (2013)

[11] M. W. Allen et al., *Polarity effects in the x-ray photoemission of ZnO and other wurtzite semiconductors*, Appl. Phys. Lett. 98, 101906 (2011)

[12] M. Gonschorek et al., *Two-dimensional electron gas density in $Al_{1-x}In_x/AlN/GaN$ heterostructures ($0.03 < x < 0.23$)*, Journal of Applied Physics 103, 093714 (2008)

[13] A. E. Romanov, *Strain-induce polarization in wurtzite III-nitride semipolar layers*, J. Appl. Phys. 100, 023522 (2006)

[14] W. Walukiewicz et al., *Optical properties and electronic structure of InN and In-rich group III-nitride alloys*, Journal of Crystal Growth 269 (2004) 119-127

[15] J. R. Meyer, I. Vurgaftman, *Band parameters for nitrogen-containing semiconductors*, J. Appl. Phys. 94 n. 6 (2003)

[16] M. César et al., *Band gap of $In_xGa_{1-x}N$: A first principles analysis,* Appl. Phys. Lett. 98, 202107 (2011)

[17] S. Pandey et al., *Band bowing and Si donor levels in InGaN layers investigated by surface photo voltage spectroscopy,* Appl. Phys. Lett. 102, 142101 (2013)

[18] Cheng-TaiKuoet al., *Is electron accumulation universal at InN polar surfaces?,* Appl. Phys. Lett. 98, 052101 (2011)

[19] V. Darakchieva et al., *Electron accumulation at nonpolar and semipolar surfaces of wurtzite InN from generalized infrared ellipsometry,* Appl. Phys. Lett. 95, 202102 (2009)

[20] T. D. Veal et al., *Transition from electron accumulation to depletion at InGaN surfaces,* Appl. Phys. Lett. 89, 202110 (2006)

[21] H. Lüth, *Solid surfaces, interfaces and thin films (fifth edition)*, Springer-Verlag Berlin Heidelberg 2010

[22] T. Yamashita et al., *Surface reconstructions on GaN and InN Semipolar (20-21) Surfaces*, Japanese Journal of Applied Physics 49 (2010) 018001

[23] S. Ploch et al., *Topography of (20-21) AlGaN, GaN and InGaN layers grown by metal-organic vapor phase epitaxy*, Journal of Crystal Growth 356 (2012) 70–74

[24] R. Kucharski et al., Non-polar and semi-polar ammonothermal GaN substrates, Semicond. Sci. Technol. 27 (2012) 024007

[25] Yohei Enya et al., *531 nm Green Lasing of InGaN Based Laser Diodes on Semi-Polar (20-21) Free-Standing GaN substrates*, Appl. Phys. Express 2 (2009) 082101

[26] Kenji Fujito et al., *High-quality nonpolar m-plane GaN substrates grown by HVPE*, Phys. Stat. Sol. (a) 205 No.5 (2008)

[27] S. F. Chichibu et al., *Advantages and remaining issues of state-of-art m-plane freestanding GaN substrates grown by halide vapor phase epitaxy for m-plane InGaN epitaxial growth*, Semicond. Sci. Technol. 27 (2012) 024008

[28] E. Richter, *Growth of GaN boules via vertical HVPE*, Journal of Crystal Growth 350 (2012)

[29] A. E. Romanov, *Basal plane misfit dislocations and stress relaxation in III-nitride semipolar heteroepitaxy*, J. Appl. Phys. 109, 103522 (2011)

[30] S. Ploch et al., *Indium incorporation efficiency and critical layer thickness of (20-21) InGaN layers on GaN*, Appl. Phys. Lett. 101, 202102 (2012)

[31] E. C. Young et al., *Determination of Composition and Lattice Relaxation in Semipolar Ternary (In,Al,Ga)N Strained Layers from Symmetric X-ray Diffraction Measurements*, App. Phys. Express 4 (2011) 061001

[32] M. T. Hardy et al., *Trace analysis of non-basal plane misfit stress relaxation in (20-21) and (30-3-1) semipolar InGaN/GaN heterostructures*, App. Phys. Lett. 100, 202103 (2012)

[33] D. A. Browne et al., *Indium and impurity incorporation in InGaN films on polar, nonpolar, and semipolar GaN orientations grown by ammonia molecular beam epitaxy*, J. Vac. Sci. Technol. A 30, 041513 (2012).

[34] J. C. Rass, *Charakterisierung von InGaN-basierten Lichtemittern auf semipolaren und nichtpolaren Halbleiteroberflächen*, phd thesis 2012

[35] T. Wernicke et al., *Indium incorporation and emission wavelength of polar, nonpolar and semipolar InGaN quantum wells*, Semicond. Sci. Technol. 27 (2012) 024014

[36] M. H. Hablanian, *High-Vacuum Technology: a practical guide (second edition)*, 1997 by Marcel Dekker, Inc.

[37] D. Briggs, M. P. Seah, *Practical surface analysis by Auger and XPS*, 1983 John Wiley & Sons

[38] J. Falta et al., *Cleaning and growth morphology of GaN and InGaN surfaces*, Phys. Stat. Sol. B 248, No. 8, 1800 (2011)

[39] S. Hofmann, *Auger- and X-ray Photoelectron Spectroscopy in Materials Science (A User-oriented Guide)*, Springer-Verlag Berlin Heidelberg 2013

[40] Casa XPS Manual 2.3.15 Rev 1.2, 2009 Casa Software Ltd

[41] V. L. Mironov, *Fundamentals of scanning probe microscope*, NT-MDT 2004

[42] www3.physik.uni-greifswald.de

[43] C. Bai, *Scanning Tunneling Microscopy and Its Applications (Second, Revised Edition)*, Shangai Scientific & Technical Publishers and Springer-Verlag Berlin Heidelberg 2000

[44] S. Ernst, *Optimisation of the preparation process for tips used in scanning tunneling microscopy*, phd thesis 2006

[45] L. Kronik, Y. Shapira, *Surface Photovoltage spectroscopy of semiconductor structures: at the crossroads of physics, chemistry and electrical enrineering*, Surf. Interface Anal. 2001; 31: 954

[46] A. Cavallini et al., *Photocurrent and Surface Photovoltage Spectroscopy Investigations of CdTe-Based Compounds*, IEEE vol.54 no.5 (2007)

[47] L. H. Germer, *Low energy electron diffraction*, Physics Today July 1964

[48] Craig A. Gerken, *Characterization of materials (second edition)*, Published online 15 OCT 2002

[49] I. Koslow, "private communication", Institut of solid state physics TU Berlin

[51] Ph. Ebert et al., *Direct measurement of the band gap and Fermi level position at InN(11-20)*, Appl. Phys. Lett. 98, 062103 (2011)

[50] Scanning Tunneling Microscopy (Specific Assignment: STM study of HOPG and Gold films), Nue Unique 2009 Laboratory Program

Acknowledgement

First of all I would like to acknowledge my Italian tutor Prof. Daniela Cavalcoli for the opportunity to write this thesis. She supported me in the best way. He gave me valuable tips and made helpful observations, and on the same time she left me autonomy in the organization of this work.

Then I would to acknowledge Michael Kneissl for the opportunity to perform the most part of the measurements and experimental part of the thesis in his outstanding research group at the Technical University of Berlin.

I want to acknowledge my German tutor Prof. Patrick Vogt for cooperative discussions, comments and observations about my experimental results.

Special thanks are devoted to the phd student Daria Skuridina for the the systematic support of my activity, i.e. the explanation of several experimental methods and the discussion of several tips to optimize both the analysis and the presentation of the experimental results.

Thanks also to Thomas, my roommate in Berlin, a nice person who allowed a serene and enjoyable living during my internship activity.

Finally, thanks to my family who was always patient with me.